Athens Journal of Technology & Engineering

Quarterly Academic Periodical, Volume 12, Issue 3
Published by the Athens Institute
URL: https://www.athensjournals.gr/ajte Email: journals@atiner.gr
e-ISSN: 2241-8237 DOI: 10.30958/ajte

Athens Journal of Technology & Engineering

Quarterly Academic Periodical, Volume 12, Issue 3, September 2025

Published by the Athens Institute

URL: https://www.athensjournals.gr/ajte Email: journals@atiner.gr

Athens Journal of Technology & Engineering

Published by the Athens Institute

Athens Institute is an Athens-based World Association of Academics and Researchers based in Athens. Athens Institute is an independent and non-profit Association with a Mission to become a forum where Academics and Researchers from all over the world can meet in Athens, exchange ideas on their research and discuss future developments in their disciplines, as well as engage with professionals from other fields. Athens was chosen because of its long history of academic gatherings, which go back thousands of years to Plato's Academy and Aristotle's Lyceum. Both these historic places are within walking distance from Athens Institute's downtown offices. Since antiquity, Athens was an open city. In the words of Pericles, Athens"…is open to the world, we never expel a foreigner from learning or seeing". ("Pericles' Funeral Oration", in Thucydides, The History of the Peloponnesian War). It is Athens Institute's mission to revive the glory of Ancient Athens by inviting the World Academic Community to the city, to learn from each other in an environment of freedom and respect for other people's opinions and beliefs. After all, the free expression of one's opinion formed the basis for the development of democracy, and Athens was its cradle. As it turned out, the Golden Age of Athens was in fact, the Golden Age of the Western Civilization. Education and (Re)searching for the 'truth' are the pillars of any free (democratic) society. This is the reason why Education and Research are the two core words in Athens Institute's name.

The *Athens Journal of Technology & Engineering (AJTE)* is an Open Access quarterly double-blind peer reviewed journal and considers papers from all areas engineering (civil, electrical, mechanical, industrial, computer, transportation etc), technology, innovation, new methods of production and management, and industrial organization. Many of the papers published in this journal have been presented at the various conferences sponsored by the Engineering & Architecture Division of the Athens Institute. All papers are subject to Athens Institute's Publication Ethical Policy and Statement.

Athens Journal of Technology & Engineering
ISSN NUMBER: 2241-8237 - DOI: 10.30958/ajte
Volume 12, Issue 3, September 2025
Download the entire issue (PDF)

Athens Journal of Technology & Engineering

Editorial and Reviewers' Board

President's Message

All Athens Institute's publications including its e-journals are open access without any costs (submission, processing, publishing, open access paid by authors, open access paid by readers etc.) and is independent of presentations at any of the many small events (conferences, symposiums, forums, colloquiums, courses, roundtable discussions) organized by Athens Institute throughout the year and entail significant costs of participating. The intellectual property rights of the submitting papers remain with the author. Before you submit, please make sure your paper meets the basic academic standards, which includes proper English. Some articles will be selected from the numerous papers that have been presented at the various annual international academic conferences organized by the different divisions and units of the Athens Institute for Education and Research. The plethora of papers presented every year will enable the editorial board of each journal to select the best, and in so doing produce a top-quality academic journal. In addition to papers presented, Athens Institute will encourage the independent submission of papers to be evaluated for publication.

The current issue is the third of the twelfth volume of the *Athens Journal of Technology & Engineering (AJTE)*, published by the Engineering & Architecture Division of Athens Institute.

Gregory T. Papanikos
President
Athens Institute

16th Annual International Conference on Civil Engineering
22-26 June 2026, Athens, Greece

The Civil Engineering Unit of ATINER is organizing its **16th Annual International Conference on Civil Engineering, 22-26 June 2026, Athens, Greece** sponsored by the Athens Journal of Technology & Engineering. The aim of the conference is to bring together academics and researchers of all areas of Civil Engineering other related areas. You may participate as stream leader, presenter of one paper, chair of a session or observer. Please submit a proposal using the form available (https://www.atiner.gr/2026/FORM-CIV.doc).

Academic Members Responsible for the Conference

- **Dr. Dimitrios Goulias**, Head, Civil Engineering Unit, ATINER and Associate Professor & Director of Undergraduate Studies Civil & Environmental Engineering Department, University of Maryland, USA.

Important Dates

- Abstract Submission: **18 November 2025**
- Acceptance of Abstract: 4 Weeks after Submission
- Submission of Paper: **25 May 2026**

Social and Educational Program

The Social Program Emphasizes the Educational Aspect of the Academic Meetings of Athens Institute.

- Greek Night Entertainment (This is the official dinner of the conference)
- Athens Sightseeing: Old and New-An Educational Urban Walk
- Social Dinner
- Mycenae Visit
- Exploration of the Aegean Islands
- Delphi Visit

Conference Fees

Conference fees vary from 400€ to 2000€
Details can be found at: https://www.atiner.gr/fees

Athens Institute for Education and Research
A World Association of Academics and Researchers

14th Annual International Conference on Industrial, Systems and Design Engineering, 22-26 June 2026, Athens, Greece

The Industrial Engineering Unit of ATINER will hold its **14th Annual International Conference on Industrial, Systems and Design Engineering, 22-26 June 2026, Athens, Greece** sponsored by the Athens Journal of Technology & Engineering.The aim of the conference is to bring together academics, researchers and professionals in areas of Industrial, Systems, Design Engineering and related subjects. You may participate as stream leader, presenter of one paper, chair of a session or observer. Please submit a proposal using the form available (https://www.atiner.gr/2026/FORM-IND.doc).

Important Dates

- Abstract Submission: **18 November 2025**
- Acceptance of Abstract: 4 Weeks after Submission
- Submission of Paper: **25 May 2026**

Academic Member Responsible for the Conference

- **Dr. Theodore Trafalis**, Director, Engineering & Architecture Division, ATINER, Professor of Industrial & Systems Engineering and Director, Optimization & Intelligent Systems Laboratory, The University of Oklahoma, USA.

Social and Educational Program

The Social Program Emphasizes the Educational Aspect of the Academic Meetings of Athens Institute.

- Greek Night Entertainment (This is the official dinner of the conference)
- Athens Sightseeing: Old and New-An Educational Urban Walk
- Social Dinner
- Mycenae Visit
- Exploration of the Aegean Islands
- Delphi Visit
- Ancient Corinth and Cape Sounion

More information can be found here: https://www.atiner.gr/social-program

Conference Fees

Conference fees vary from 400€ to 2000€

Details can be found at: https://www.atiner.gr/fees

Athens Journal of Technology and Engineering - Volume 12, Issue 3, September 2025 – Pages 143-160

Segregation-Resistant Carbon Microfibre Reinforced Self-Consolidating Concrete

By Md. Safiuddin, Fraser Zenwirt±, Moe Shammakh°, Rasha Al-Attar•, Baryalai Sharifi♦ & Peter Tumidajski♥*

This paper presents the segregation resistance and flowability of self-consolidating concrete (SCC) including carbon microfibres. Initially, six SCCs were produced incorporating 0–0.50 vol.% of carbon microfibres at the two water-to-binder (W/B) ratios of 0.40 and 0.50. Later, two more SCCs were prepared using viscosity-modifying admixture (VMA) with 0% and 0.25% carbon microfibres at the W/B ratio of 0.40 for further improvement of segregation resistance. All SCCs were tested for slump flow and T_{50} flow time to determine flowability. The segregation resistance of SCCs was measured with respect to sieve segregation index (SSI). In addition, the appearance of SCCs was checked after the slump flow test to obtain visual stability index (VSI). The distribution of coarse aggregate particles in the two split halves of Ø100 mm x 200 mm cylinders was also examined as another indicator of the segregation resistance of SCC. Test results revealed that the SCCs made with the W/B ratio of 0.40 had excellent segregation resistance and good flowability. Carbon microfibres significantly decreased the flowability of SCC but increased its segregation resistance. Therefore, slump flow and SSI were lower whereas T_{50} flow time was higher for the SCCs with carbon microfibres. Moreover, the VSI of SCC became better with the inclusion of carbon microfibres. VMA further improved the SSI and VSI of SCC through enhanced viscosity. The distribution of coarse aggregate particles was also more uniform in the SCCs including carbon microfibres with or without VMA. Overall, the best performance of SCC with respect to both segregation resistance and flowability was observed for 0.25% carbon microfibres.

Keywords: *carbon microfibres, flowability, segregation resistance, self-consolidating concrete, viscosity-modifying admixture.*

Introduction

Self-consolidating concrete (SCC) is a highly flowable material that spreads through congested reinforcement and fills every corner of the formwork under self-weight without requiring any external compaction efforts such as vibration (Safiuddin 2008, Santos et al. 2017). It is a good choice for many structural elements where placing and compaction of ordinary concrete can be difficult due to the complex shape

---

*Professor, Centre for Construction and Engineering Technologies, George Brown College, Canada.
±Student Researcher, Centre for Construction and Engineering Technologies, George Brown College, Canada.
°Student Researcher, Centre for Construction and Engineering Technologies, George Brown College, Canada.
•Professor, Centre for Construction and Engineering Technologies, George Brown College, Canada.
♦Student Researcher, Centre for Construction and Engineering Technologies, George Brown College, Canada.
♥Associate Dean, Centre for Construction and Engineering Technologies, George Brown College, Canada.

of formwork and congested reinforcement. The key workability properties of SCC are flowability and segregation resistance (Safiuddin, West et al. 2010). The merits of SCC depend on its flowability and segregation resistance. SCC must possess excellent flowability and adequate segregation resistance for good performance after being used in structures. However, SCC may suffer from inadequate or excessive flowability and poor segregation resistance if not designed properly (see Figure 1). In such case, SCC might exhibit segregation in the forms of bleeding, paste or mortar separation, and non-uniform distribution of coarse aggregates, which affect the properties and durability of hardened concrete (Safiuddin et al. 2009).

Figure 1. *Poor Segregation Resistance of SCC*

SCC was invented in Japan in 1980s to resolve the shortage of skilled labourers and to enhance the durability of concrete (Okamura & Ozawa 1995). It was initially developed using a high-range water reducer or superplasticizer (SP) and higher contents of cement and fine aggregate but a lower amount of smaller-size coarse aggregate with no fibres (Ashish & Verma 2019, Okamura & Ozawa 1995, Okamura 1997, Okamura & Ouchi 2003). Fibre-reinforced SCC is a relatively new development in concrete technology. The foremost aim of including fibres in SCC is to increase the ductility, thus overcoming its inherent deficiency of high brittleness. The fibres arrest the cracks and allow much larger deformation of concrete beyond the peak stress (Barluenga & Hernández-Olivares 2007). Hence, the inclusion of randomly distributed fibres in SCC would increase its tensile strength, stiffness, ductility, and toughness by preventing or controlling the initiation, propagation, and connectivity of cracks.

The use of fibres might also increase the segregation resistance of SCC through reductions in bleeding, paste or mortar separation, and aggregate settlement. However, the incorporation of fibres into SCC is a big challenge, since they significantly lessen the flowability of concrete (Yakhlaf et al. 2013). Yet many studies have been conducted to include different types of fibres in SCC. A literature review revealed that several researchers used steel, glass, and polypropylene fibres in SCC without adversely affecting its flowability (Corinaldesi & Moriconi 2004, Torrijos et al. 2008).

Also, few studies showed that steel and glass fibres can be used in producing SCC with an increased resistance to segregation (Barluenga & Hernández-Olivares 2007, Grünewald & Walraven 2001). In comparison, limited research was conducted to produce SCC using carbon microfibres, although the inclusion of such fibres in non-self-consolidating concrete is not completely new.

There is a potential for producing SCC with carbon microfibres, which could eliminate the shortcomings of other fibres. Steel fibres can cause corrosion problems when exposed on the surface of concrete (Safiuddin 2003). Glass fibres may suffer from embrittlement and strength loss (Safiuddin, Abdel-Sayed et al. 2010). Polypropylene fibres have some drawbacks such as poor fire resistance, low modulus of elasticity, low bond strength and high sensitivity to sunlight, although they are chemically inert and stable in the alkaline environment of concrete (Safiuddin, Abdel-Sayed et al. 2010). Carbon microfibres can be used to overcome these drawbacks. They are very attractive for their superior chemical stability at ambient temperatures. Carbon fibres are inert, physically as strong as steel fibres, and chemically more stable than glass and polypropylene fibres in an alkaline environment (Safiuddin 2003). They possess much higher modulus of elasticity and better thermal resistance than polypropylene fibres. Carbon fibres are also lighter and their strength-to-density ratio is higher than many other fibres (Safiuddin, Abdel-Sayed et al. 2010). Furthermore, the benefits of carbon microfibres could be enhanced by using ultrafine supplementary cementing materials such as silica fume (Yakhlaf 2013, Safiuddin et al. 2018).

The above-mentioned benefits of carbon microfibres might not be realized for SCC unless its flowability and segregation resistance are adequately achieved. Hence, experimental research should be carried out to investigate the effects of carbon microfibres on the flowability and segregation resistance of SCC. In this perspective, carbon microfibres obtained from recycled carbon-fibre-reinforced polymers can be used with sustainability benefits. Moreover, viscosity-modifying admixture (VMA) is known to improve the segregation resistance of SCC (Lachemi et al. 2004, Piekarczyk & Ła´zniewska-Piekarczyk 2021). VMA can be used additionally to produce segregation-resistant carbon microfibre reinforced SCC (CMFRSCC). For this, the synergistic effect of VMA and carbon microfibres on the segregation resistance of SCC should also be investigated. The present research was performed to produce CMFRSCC with excellent segregation resistance, while maintaining good flowability. The research tasks were carried out through selection of constituent materials, design of concrete mixtures, and testing of different fresh and hardened CMFRSCCs to examine the effects of carbon microfibres and VMA on the flowability and segregation resistance of concrete. Based on the experimental results, the optimum content of carbon microfibres was determined.

Research Significance

The outcomes of this study will create new opportunities for the construction industry. The research findings are expected to promote the production of CMFRSCC and accelerate its usage in new construction, precast concrete elements (wall panels, spandrel panels, decorative frames, etc.), and repair or rehabilitation work. The application of CMFRSCC in the repair or rehabilitation of aged structures will decrease the demands of cement and aggregates through a significant reduction in the required amount of concrete for new construction. Consequently, this will reduce the environmental pollution caused by aggregate harvesting from quarries and CO_2 emissions from cement factories. The usage of CMFRSCC will also reduce the ultimate quantity of construction and demolition wastes. Moreover, CMFRSCC was produced in this study by using Portland limestone cement, silica fume, and carbon microfibres. The manufacturing of Portland limestone cement declines the carbon footprint of cement factories by about 10%. In addition, silica fume is generated as a by-product of the silicon and ferrosilicon industries. Also, carbon microfibres used in this study are manufactured from recycled carbon-fibre-reinforced polymers. Hence, the use of these materials in CMFRSCC will help to mitigate the waste disposal and air pollution issues, thus contributing to environmental sustainability.

Experimental Materials and Methods

Concrete Materials

General-use Portland limestone (CSA Type GUL) cement, pea gravel (10 mm nominal maximum size), pit sand (5 mm nominal maximum size), carbon microfibres, densified silica fume, polycarboxylate-based SP, VMA, and normal tap water were used in the present study. Carbon microfibres (CMF) manufactured from recycled carbon-fibre-reinforced polymers were used, as they are less expensive and more sustainable than virgin carbon fibres. Pea gravel was used as coarse aggregate (CA) and pit sand was used as fine aggregate (FA). Type GUL cement (C) was used as the main binding material whereas silica fume (SF) was used as a supplementary cementing material. SF was used to ensure that the minimum specified compressive strength at 28 days is achieved, particularly as required for various chloride and freezing exposures described in CSA A23.1:19/CSA A23.2:19. It also aided the dispersion of CMF in concrete mixtures. SP was used in all concrete mixtures to obtain the required flowability of SCC. Tap water (W) was suitable for making concrete mixtures. In addition, VMA was used in two selected concrete mixtures for enhanced segregation resistance. Some of the physical properties of the constituent materials are given in Table 1.

Most of the properties presented in Table 1 were used to judge the suitability of the constituent materials and to determine the mixture proportions of concretes. Both fine and coarse aggregates satisfied the grading requirements of CSA A23.1: 19/CSA A23.2:19. The sieve analysis results of pit sand and pea gravel are shown in Table 2. The fineness modulus of sand was 2.7 whereas it was 5.9 for gravel. Cement and SF fulfilled the specified physical and chemical requirements. The fineness of cement fulfilled the requirements as specified in CSA A3001-13. The limestone content of the cement was 9.5%. The chemical compositions of cement and SF are shown in Table 3. SF was very rich in silica content. It fulfilled the minimum requirement of SiO_2 (85%) specified in ASTM C1240-20. The SO_3 concentration and loss on ignition (LOI) of the cement were below the maximum limits as stated in ASTM C595/C595M-21.

Table 1. *Physical Properties of the Constituent Materials of Concretes*

Constituent Material	Properties
Portland limestone cement*	Specific gravity: 3.11, Percent passing 45-μm sieve: 98.9%, Blaine specific surface area: 445 m^2/kg
Pea gravel	Specific gravity: 2.66, Absorption: 1.2%
Pit sand	Specific gravity: 2.66, Absorption: 1.4%
Silica fume†	Median particle size: 8 μm, Specific gravity: 2.24
Carbon microfibres‡	Fibre length: 6 mm, Fibre diameter: 7 μm Specific gravity: 1.80
Superplasticizer†	Specific gravity: 1.08, Solid content: 36%
Viscosity-modifying admixture†	Specific gravity: 1.02
Tap water	Density: 997.5 kg/m^3

*Properties were acquired from Lafarge Canada Inc. †Properties were sourced from Sika Canada Inc. ‡Properties were obtained from ELG Carbon Fibre Ltd.

Table 2. *Gradations of Pea Gravel and Pit Sand*

Pea Gravel		
Sieve Size	**Mass Percent Passing**	**CSA Limits**
14 mm	100	100
10 mm	91	85–100
5 mm	10.9	10–30
2.5 mm	3.5	0–10
1.25 mm	1.5	0–5
Pit Sand		
Sieve Size	**Mass Percent Passing**	**CSA Limits**
10 mm	100	100
5 mm	97.6	95–100
2.5 mm	82.4	80–100
1.25 mm	68.6	50–90
630 μm	51.7	25–65
315 μm	24.1	10–35
160 μm	6.6	2–10

Table 3. *Chemical Compositions of Cement and Silica Fume*

Chemical Component	Mass Content (%)	
	Cement*	Silica Fume†
Calcium oxide (CaO)	62.8	< 2%
Silicon dioxide (SiO_2)	19.0	≥ 90% > 85% (ASTM limit)
Aluminum oxide (Al_2O_3)	4.6	–
Iron oxide (Fe_2O_3)	3.0	–
Sulphur trioxide (SO_3)	2.8 ≤ 4.0% (ASTM limit)	–
Magnesium oxide (MgO)	0.8	–
Free CaO	1.0	–
Equivalent sodium oxide (Na_2O_{eq})	0.49	–
Limestone ($CaCO_3$) addition	9.5	–
Loss on ignition (LOI)	5.0 ≤ 10.0% (ASTM limit)	–

*Chemical composition was obtained from Lafarge Canada Inc. †Chemical composition was sourced from Sika Canada Inc.

Concrete Mixture Proportions

In total, eight SCC mixtures were designed and prepared in this study. Initially, six SCC mixtures were produced based on the water-to-binder (W/B) ratios of 0.40 and 0.50, and using 0%, 0.25% and 0.50% CMF by volume of concrete. Later, two additional SCC mixtures were produced using VMA along with 0% and 0.25% CMF at the W/B ratio of 0.40. In all concrete mixtures, SF was used by replacing 5% of the cement by weight. The guidelines of American Concrete Institute (ACI PRC-237-07) were followed to determine the mixture proportions of C, W, SF, FA, CA, and CMF. SP and VMA dosages were fixed based on the flowability and segregation resistance or stability of trial batches. A minimum slump flow of 550 mm as a measure of acceptable flowability and a maximum sieve segregation index of 18% for adequate stability were targeted for the SCC mixtures. The details of concrete mixture proportions are shown in Table 4.

Table 4. *Concrete Mixture Proportions*

Mixture Designation	W/B Ratio	CMF		C	SF	W	FA	CA	SP	VMA
		Vol. %	kg/m^3	kg/m^3	kg/m^3	kg/m^3	kg/m^3	kg/m^3	% B	% B*
CGUL40CF0	0.40	0	0	443.7	23.3	186.8	836.0	836.0	1.000	–
CGUL40CF25	0.40	0.25	4.5	443.7	23.3	186.8	829.4	836.0	4.250	–
CGUL40CF50	0.40	0.50	9.0	443.7	23.3	186.8	822.8	836.0	7.500	–
CGUL50CF0	0.50	0	0	392.8	20.7	206.8	836.0	836.0	0.625	–
CGUL50CF25	0.50	0.25	4.5	392.8	20.7	206.8	829.4	836.0	3.750	–
CGUL50CF50	0.50	0.50	9.0	392.8	20.7	206.8	822.8	836.0	7.000	–
CGUL40CF0V	0.40	0	0	443.7	23.3	186.8	836.0	836.0	1.000	0.118
CGUL40CF25V	0.40	0.25	4.5	443.7	23.3	186.8	829.4	836.0	4.750	0.118

*C + SF

Preparation and Testing of Concretes

Fresh concretes were prepared using a pan-type shear mixer as illustrated in Figure 2. At first, pea gravel and pit sand were charged and mixed with the first one-third of the mixing water for 1 minute. Then the mixer was stopped, the binding materials (cement plus silica fume) were incorporated, and the mixing was continued for 2 minutes after adding the second one-third of the mixing water blended with half of the SP dosage. Thereafter, the mixer was stopped and carbon microfibres were spread by hand followed by 1 minute of mixing – this step was omitted in the cases of the control concretes without fibres. After that, the final one-third of the mixing water blended with the remaining half of the SP dosage was added and the mixer was run further for 2 minutes. When needed, an additional mixing of 1 minute or 2 (1 + 1) minutes was adopted by judging the flowability of concrete, particularly in the presence of carbon microfibres.

Immediately after the completion of mixing, the fresh concretes were discharged from the mixer into a steel tray, and tested for flowability and segregation resistance. The flowability of the concretes was determined with respect to slump flow and T_{50}

flow time following the procedures given in ASTM C1611/C1611M-21. The slump flow of the concretes was measured using an Abram's cone in its inverted position on a levelled baseplate (refer to Figure 3). The inverted cone was filled with freshly mixed concrete in one lift and without any compaction. Then the cone was raised vertically and the flow time of the concrete sample to spread 50 cm (T_{50}) was measured by a stopwatch. In addition, the largest and associated perpendicular diameters of the concrete spread (refer to Figure 3) at the end of the slump flow test were measured. The average diameter was recorded as the slump flow.

Figure 2. *Post-mixed Fresh Concrete*

Figure 3. *T_{50} Flow Time and Slump Flow Test for Flowability*

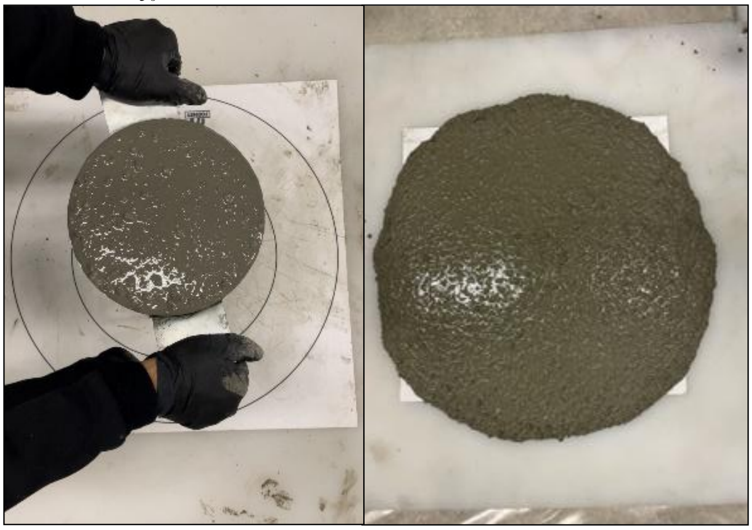

The segregation resistance of the concretes was measured using a 300-mm diameter No. 4 sieve according to the procedure depicted in Safiuddin et al. (2012). About 2 L of fresh concrete filled in a cylindrical container was poured onto the sieve placed on a pan. After 2 minutes of resting time, the measurements for the weights of the entire concrete sample and the mortar fraction passing No. 4 sieve were taken. Then sieve segregation index (SSI) was calculated using the following equation:

$$SSI = \frac{W_m}{W_c} \times 100\%$$

where
W_m = weight of the mortar fraction passing No. 4 sieve
W_c = weight of the entire concrete sample

The segregation resistance of the concretes was also visually assessed after conducting the slump flow test and expressed in terms of visual stability index (VSI). As a qualitative measure of segregation resistance, the VSI of the concretes was determined based on their appearance in respect of bleeding, mortar halo, and aggregate pile. While deriving VSI, the criteria shown in Figure 4, as given in ASTM C1611/C1611M-21, were used. Along with SSI and VSI, the distribution of coarse aggregate (pea gravel) particles in hardened concrete was also observed as another qualitative measure of segregation resistance. For this purpose, the two halves of Ø100 mm x 200 mm cylinder specimens after splitting longitudinally at the age of 28 days (Figure 5) were visually examined. The presence of pea gravel on the split faces was checked and photographed to judge the segregation resistance of concrete.

Figure 4. *Criteria for Visual Stability Index of Concrete*

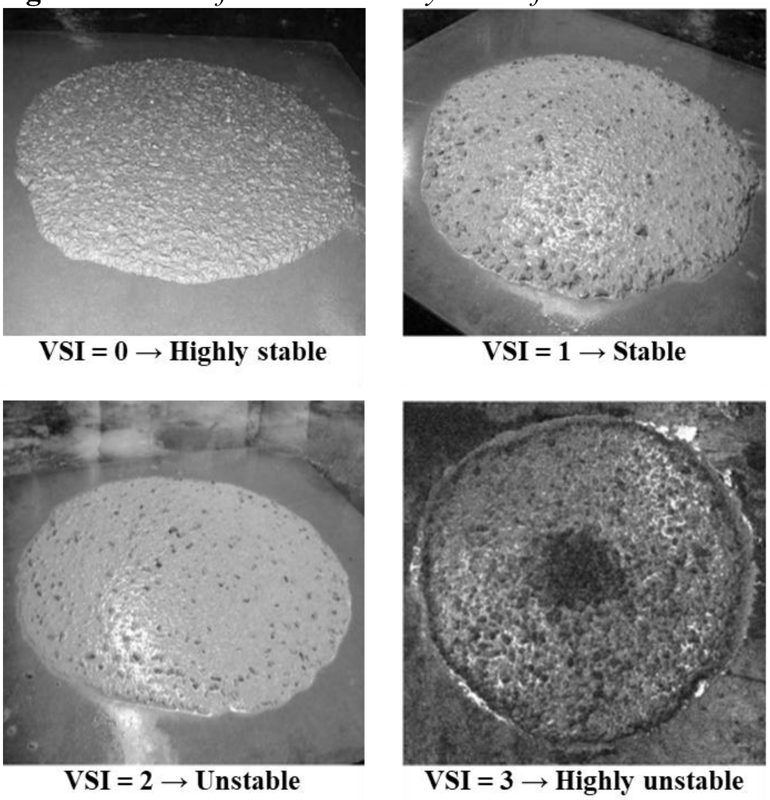

VSI = 0, no evidence of segregation or bleeding.
VSI = 1, no evidence of segregation but slight bleeding observed as a sheen on the concrete mass.
VSI = 2, a slight mortar halo ≤ 10 mm and/or aggregate pile in the center of the concrete mass.
VSI = 3, clearly segregating by evidence of a large mortar halo > 10 mm and/or a large aggregate pile in the center of the concrete mass.

Figure 5. *Two Halves of a Cylinder Specimen after Splitting*

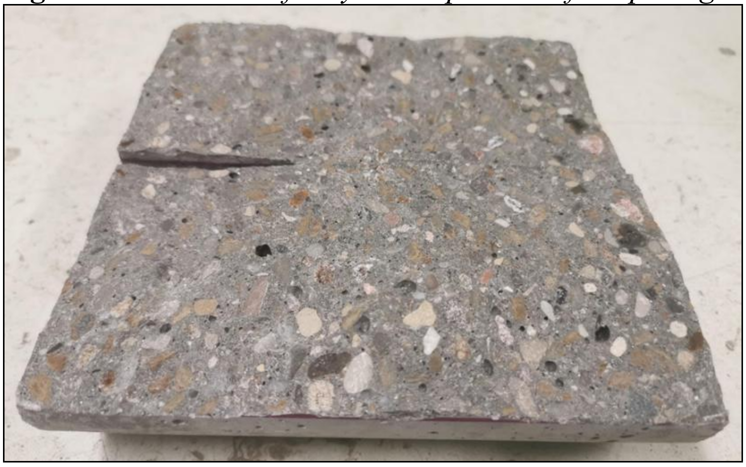

Test Results and Discussion

The concretes were tested to determine their flowability (slump flow and T_{50} flow time) and segregation resistance (SSI) quantitatively. The segregation resistance of the concretes was also qualitatively examined with respect to the VSI of fresh samples and the distribution of coarse aggregate particles in hardened cylinder specimens. Experimental results were analyzed to determine the effects of carbon microfibres, W/B ratio, and VMA on the flowability and segregation resistance of SCC as well as to derive the optimum fibre content for CMFRSCC.

Flowability of Concretes

The flowability results in terms of slump flow and T_{50} flow time are shown in Table 5. All concretes provided a slump flow greater than 550 mm, which is the minimum acceptable value for SCC (Islam et al. 2022, SCCEPG 2005). The T_{50} flow time values of the concretes were comparatively high, except for CGUL50CF0. A T_{50} flow time less than 7 s is typically required for SCC (Islam et al. 2022). However, it is advised to set the T_{50} flow time more broadly for SCC (Koehler & Fowler 2007). This is because the SCC mixtures with a wide range of T_{50} flow time can be placed successfully. Moreover, it should be mentioned that a T_{50} flow time less than 7 s was suggested for the SCCs made without fibres. In the present study, the T_{50} flow time was recorded for the concretes with 0%, 0.25%, and 0.50% carbon microfibres. The concrete mixtures including 0.25% and 0.50% carbon microfibres provided a T_{50} flow time $\geq$ 11.5 s. Conversely, the control concrete mixtures without any fibres had a T_{50} flow time $\leq$ 9.3 s.

Table 5. *Flowability Results of Various Concretes*

Mixture Designation	W/B Ratio	CMF		SP	VMA	Slump Flow (mm)	T_{50} Flow Time (s)
		Vol. %	kg/m^3	% B	% B*		
CGUL40CF0	0.40	0	0	1.000	–	675	9.3
CGUL40CF25	0.40	0.25	4.5	4.250	–	625	13
CGUL40CF50	0.40	0.50	9.0	7.500	–	645	14
CGUL50CF0	0.50	0	0	0.625	–	660	4.1
CGUL50CF25	0.50	0.25	4.5	3.750	–	575	11.5
CGUL50CF50	0.50	0.50	9.0	7.000	–	580	13
CGUL40CF0V	0.40	0	0	1.000	0.118	605	15.4
CGUL40CF25V	0.40	0.25	4.5	4.750	0.118	615	17.7

*C + SF

The incorporation of carbon microfibres significantly decreased the flowability of concrete, as demonstrated by lower slump flow and higher T_{50} flow time. Similar results were found in earlier research (Yakhlaf 2013, Yakhlaf et al. 2013). The SCC mixtures with carbon microfibres provided a lower slump flow and a higher T_{50} flow time. These flow results are related to the greater surface area of total solid materials in the presence of carbon microfibres. The wettable surface area increased and therefore the water demand became higher for the targeted slump flow. However, as the water content was kept constant (refer to Table 4), high SP dosages were needed to achieve a slump flow greater than 550 mm (refer to Table 5). Polycarboxylate-based SP improved the flowability of concrete. It helped to disperse the binder (cement and silica fume) particles and carbon microfibres by its repelling and steric hindrance actions. The SP dosage increased with a higher content of carbon microfibres. The largest SP dosage was required for 0.50% carbon microfibres. It should be noted that the SP dosage for 0.50% carbon microfibres was extremely high as compared to the recommended amount given by the manufacturer for non-fibre-reinforced SCC. This is due to the greater surface area and volume concentration of fibres which increased the water demand for the targeted slump flow ($\geq$ 550 mm). Furthermore, the larger SP dosages were needed for the concretes made with the W/B ratio of 0.40. This is because the binder content was higher whereas the water content was lower for these concretes.

The concretes made with the W/B ratio of 0.40 provided higher slump flow and T_{50} flow time, as evident from Table 5. This is mostly due to the relatively high cohesiveness of concrete which was linked with the proportions of cement, silica fume, and water. It can be seen from Table 4 that the coarse aggregate (pea gravel) content remained the same for all concretes. In comparison, the fine aggregate (pit sand) content slightly decreased with the inclusion of carbon microfibres. This is because the amount of carbon microfibres was considered in the concrete mixture design by replacing an equal volume of pit sand. Nevertheless, the corresponding concretes with the same amount of carbon microfibres had the equal sand content. In general, the proportions of pea gravel and pit sand indicate that they did not play a dominant role in varying the cohesiveness of concrete. In contrast, the cement and silica fume contents were much higher whereas the water content was considerably lower for the concretes made with the W/B ratio of 0.40. Because of a lower water content with higher amounts of cement and silica fume, the cohesiveness of concrete increased. Consequently, the viscosity of concrete became higher which is evident from the results of T_{50} flow time. Furthermore, the deformability of concrete can be higher due to its more cohesiveness. As a result, an increase in slump flow might occur, as observed in the present study. However, it should be mentioned that very high viscosity caused by excessive cohesiveness may diminish the slump flow of concrete which was noticed for the VMA concretes in this study.

The SCC mixtures with VMA were highly cohesive as compared to the corresponding mixtures without VMA, as obvious from the results of slump flow and T_{50} flow time (see Table 5). The slump flow values of CGUL40CF0V and CGUL40CF25V were relatively low, although they remained above the targeted minimum value of 550 mm. In addition, the highest level of T_{50} flow time ($\geq$ 15.4 s) was obtained for these two SCCs. These results suggest that the viscosity of concrete increased substantially when VMA was used. Therefore, the flowability of SCC decreased and a higher SP dosage was needed for the targeted slump flow, particularly in the presence of carbon microfibres.

Segregation Resistance

The results obtained from the sieve segregation test and visual observation of slump flow spreads (SSIs and VSIs) are given in Table 6. The slump flow spreads assessed for the VSIs of different concretes are also shown in Figure 6 and Figure 7. Generally, the SSI results were consistent with the VSI values. The SSI values of all concretes were greatly lower than 18%, which is the maximum allowable limit for SCC (Salam et al. 2019, Parez et al. 2002). It suggests that all SCC mixtures possessed a high segregation resistance. However, the SCC mixtures made with the W/B ratio of 0.40 exhibited more segregation resistance providing lower SSI and VSI values. This is because these SCC mixtures were produced using the higher amounts of cement and silica fume at a lower water content which increased the viscosity of concrete, as evident from the results of T_{50} flow time (refer to Table 5). The higher viscosity contributed to improving the segregation resistance of concrete.

The incorporation of carbon microfibres increased the segregation resistance of concrete, as evident from the SSI and VSI values given in Table 6. Both SSI and VSI became lower with the higher amount of carbon microfibres in SCC, thus indicating a better segregation resistance. When no VMA was used, the lowest SSI and VSI values were obtained for 0.50% carbon microfibres. The improvement in segregation resistance by carbon microfibres was particularly more pronounced for the concretes prepared with the W/B ratio of 0.40 (see Table 6). The segregation resistance of concrete was enhanced by carbon microfibres because of reduced fluidity. The slump flow of concrete decreased whereas its T_{50} flow time increased with the higher content of carbon microfibres. Such results of slump flow and T_{50} flow time suggest that the flowability of concrete decreased in the presence of carbon microfibres. The decrease in concrete flowability contributed to improving the segregation resistance of SCC.

The VSI values of the concretes including carbon microfibres and VMA separately or combinedly were 0–1.00. An SCC with a VSI of ‘0’ is ‘highly stable’ whereas an SCC with a VSI of ‘1.00’ is ‘stable’ according to the criteria given in ASTM C1611/C1611M-21. Hence, the VSI values of 0–1.00 imply that the SCC mixtures including carbon microfibres and/or VMA were resistant to segregation.

However, it should be noted that an excellent segregation resistance was achieved when carbon microfibres and VMA were used together in the concrete mixture. Indeed, the combined use of carbon microfibres and VMA was highly effective to produce segregation-resistant SCC.

Table 6. *Stability or Segregation Resistance Results of Various Concretes*

Mixture Designation	W/B Ratio	CMF		SP	VMA	SSI (%)	VSI
		Vol. %	kg/m^3	% B	% B*		
CGUL40CF0	0.40	0	0	1.000	–	4.5	1.00
CGUL40CF25	0.40	0.25	4.5	4.250	–	2.2	0.50
CGUL40CF50	0.40	0.50	9.0	7.500	–	1.0	0.25
CGUL50CF0	0.50	0	0	0.625	–	5.8	1.25
CGUL50CF25	0.50	0.25	4.5	3.750	–	3.6	1.00
CGUL50CF50	0.50	0.50	9.0	7.000	–	2.9	0.75
CGUL40CF0V	0.40	0	0	1.000	0.118	2.1	0
CGUL40CF25V	0.40	0.25	4.5	4.750	0.118	1.3	0.25

*C + SF

The use of VMA greatly increased the segregation resistance of SCC. Hence, the SSI and VSI values of the two VMA concretes (CGUL40CF0V and CGUL40CF25V) were significantly lower than their corresponding non-VMA concretes (refer to Table 6 and Figure 7). Indeed, the uniformity of fresh concrete improved with lower bleeding and mortar halo for the SCC mixtures prepared with VMA. In addition, the settlement of larger coarse aggregate particles was minimized when VMA was used in SCC (see Figure 8). Therefore, the distribution of coarse aggregate was more uniform in the cylinder specimens (see Figure 9), which were fabricated using the VMA concretes with and without carbon microfibres. The enhanced viscosity resulting from VMA impeded the settlement of aggregates and thus reduced the heterogeneity in concrete. This effect became more pronounced when VMA was used in the presence of carbon microfibres.

Optimum Content of Carbon Microfibres

The overall findings of the present study revealed that segregation-resistant SCC can be produced using carbon microfibres with or without VMA. In the present study, SCC mixtures were produced incorporating 0–0.50 vol.% of carbon microfibres. The inclusion of carbon microfibres greatly increased the segregation resistance of concrete. The SSI and VSI values decreased with the higher content of carbon microfibres, thus indicating a greater segregation resistance. In particular, the SSI and VSI values were significantly low for 0.50% carbon microfibres. However, the incorporation of carbon microfibres substantially decreased the flowability of concrete. This effect was more pronounced for the SCC mixtures including 0.50% carbon microfibres. Therefore, the extremely high SP dosages were needed to achieve the required slump flow of concrete when 0.50% carbon microfibres were used. Very high SP dosages can cause undesirable bleeding and setting problems after placing fresh concrete. Hence, considering both the flowability and segregation resistance of concrete, 0.25% was decided as the optimum content of carbon microfibres. The concrete mixtures including 0.25% carbon microfibres with or without VMA provided good flowability and excellent segregation resistance.

Figure 6. *Visual Stability Index of Fresh SCC Mixtures Prepared without VMA*

CGUL40CF0 (VSI = 1.00)

CGUL50CF0 (VSI = 1.25)

CGUL40CF25 (VSI = 0.50)

CGUL50CF25 (VSI = 1.00)

CGUL40CF50 (VSI = 0.25)

CGUL50CF50 (VSI = 0.75)

Figure 7. *Visual Stability Index of Fresh SCC Mixtures Prepared with VMA*

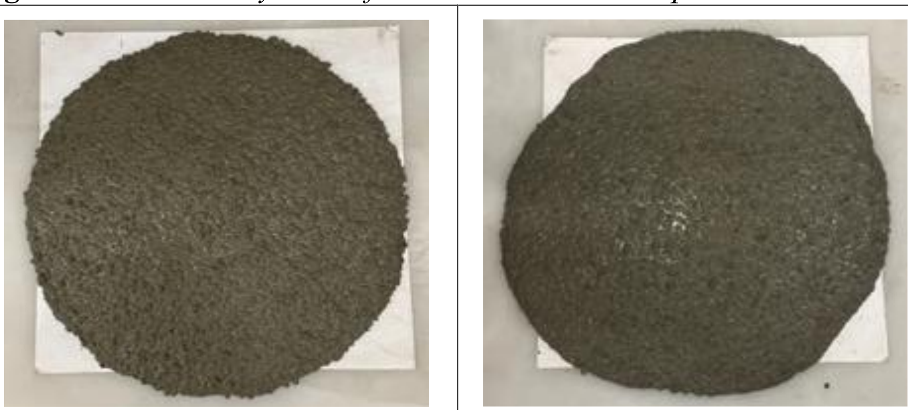

CGUL40CF0V (VSI = 0) | CGUL40CF25V (VSI = 0.25)

Figure 8. *Cylinder Specimens Cast Using SCC Mixtures Made with VMA*

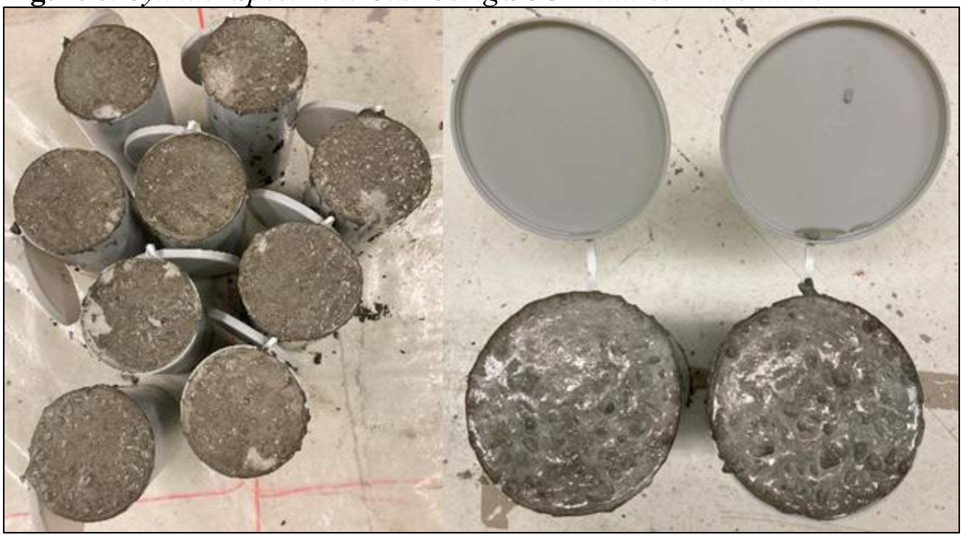

Figure 9. *Distribution of Coarse Aggregates in Hardened SCCs Prepared with VMA*

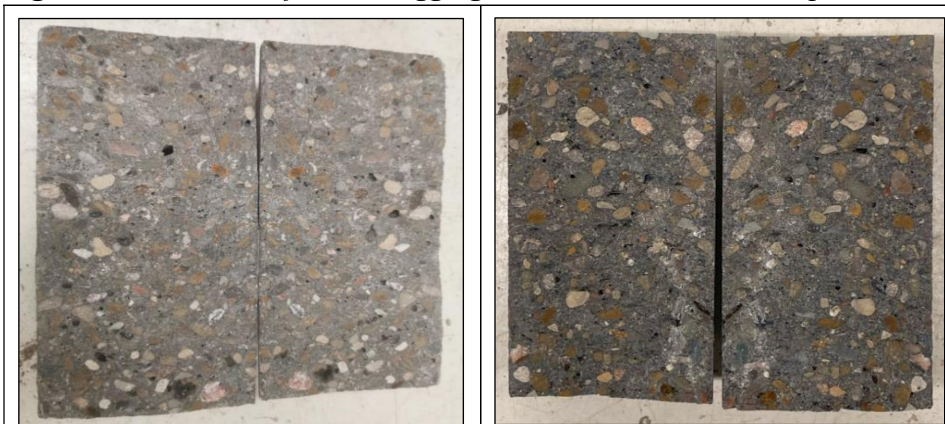

CGUL40CF0V | CGUL40CF25V

Conclusions

The following conclusions are drawn from the findings of this study on the flowability and segregation resistance of CMFRSCC.

1. Carbon microfibres, VMA, and W/B ratio notably influenced the flowability and segregation resistance of SCC.
2. The SCC mixtures made with the W/B ratio of 0.40 provided higher slump flow and T_{50} flow time due to a relatively high cohesiveness of concrete resulting from the higher amounts of cement and silica fume at a lower water content.
3. Carbon microfibres significantly decreased the flowability of concrete due to the increased surface area of total solid materials and therefore needed a higher SP dosage to achieve the targeted slump flow.
4. In the presence of carbon microfibres, slump flow decreased whereas T_{50} flow time increased with a greater fibre content, which increased the water demand, and thus needed a higher SP dosage for the required flowability of SCC.
5. Carbon microfibres greatly increased the segregation resistance of SCC due to higher viscosity resulting from the reduced fluidity of concrete.
6. The segregation resistance was higher for the SCC mixtures made with the W/B ratio of 0.40 due to the enhanced viscosity of concrete caused by the higher amounts of cement and silica fume at a lower water content.
7. Among various non-VMA CMFRSCCs, the concrete mixture prepared with the W/B ratio of 0.40 and 0.50% carbon microfibres showed the highest segregation resistance with the lowest SSI and VSI values.
8. The use of VMA decreased the flowability of SCC but greatly increased its segregation resistance due to higher viscosity.
9. An excellent improvement in the segregation resistance of SCC was observed due to the synergistic effect of VMA and carbon microfibres.
10. In the context of the present study, the optimum content of carbon microfibres was 0.25 vol.%, for which the SCC mixtures exhibited the best performance with respect to flowability and segregation resistance.

Acknowledgments

The authors express their sincere gratitude to George Brown College, Toronto, Canada, for providing the funding for the research. They are especially thankful to Alexandra Hernandez, Eva Aboagye, and Shanice Viner of the Office of Research and Innovation, George Brown College, for their contributions to accomplishing the research tasks. In addition, the authors are grateful to Bob Barham, Sika Canada Inc., for the supply of concrete admixtures. They are also thankful to Angela Ingram (Manager of Academic Operations) and Farhad Taghinia (Laboratory Coordinator), Angelo DelZotto School of Construction Management, Centre for Construction and Engineering Technologies, George Brown College, for their cooperation in the research project.

References

ACI PRC-237-07 *Self-consolidating concrete (reapproved 2019)*. Farmington Hills, MI: American Concrete Institute.

Ashish DK, Verma SK (2019) An overview on mixture design of self-compacting concrete. *Structural Concrete* 20(1): 371–395.

ASTM C595/C595M-21. *Standard specification for blended hydraulic cements*. West Conshohocken, PA: ASTM International.

ASTM C1240-20. *Standard specification for silica fume used in cementitious mixtures*. West Conshohocken, PA: ASTM International.

ASTM C1611/C1611M-21. *Standard test method for slump flow of self-consolidating concrete*. West Conshohocken, PA: ASTM International

Barluenga G, Hernández-Olivares F (2007) Cracking control modified with short AR-glass fibers at early age. Experimental results on standard concrete and SCC. *Cement and Concrete Research* 37(12): 1624–1638.

Corinaldesi V, Moriconi G (2004) Durable fiber-reinforced self-compacting concrete. *Cement and Concrete Research* 34(2): 249–254.

CSA A23.1:19/CSA A23.2:19. *Concrete materials and methods of concrete construction/ Test methods and standard practices for concrete*. Toronto, ON: Canadian Standards Association.

CSA A3001-13. *Cementitious materials for use in concrete*. Toronto, ON: Canadian Standards Association.

Grünewald S, Walraven JC (2001) Parameter-study on the influence of steel fibers and coarse aggregate content on the fresh properties of self-compacting concrete. *Cement and Concrete Research* 31(12): 1793–1789.

Islam GMS, Akter S, Reza TB (2022) Sustainable high-performance, self-compacting concrete using ladle slag. *Cleaner Engineering and Technology* 7: Article 100439.

Koehler EP, Fowler DW (2007) *Self-consolidating concrete for precast structural applications: mixture proportions, workability, and early age hardened properties (FHWA/TX-08/0-5134-1)*. Austin, TX: Center for Transportation Research, The University of Texas at Austin.

Lachemi M, Hossain KMA, Lambros V, Nkinamubanzi P-C, Bouzoubaâ N (2004) Self-consolidating concrete incorporating new viscosity modifying admixtures. *Cement and Concrete Research* 34(6): 917–926.

Okamura H (1997) Self-compacting high-performance concrete. *Concrete International* 19(7): 50–54.

Okamura H, Ouchi M (2003) Self-compacting concrete. *Journal of Advanced Concrete Technology* 1(1): 5–15.

Okamura H, Ozawa K (1995) Mix design for self-compacting concrete. *Concrete Library of JSCE* 25(6): 107–120.

Parez N, Romero H, Hermida G, Cuellar G (2002) Self-compacting concrete, on the search and finding of an optimized design. In *Proceedings of the First North American Conference on the Design and Use of Self-Consolidating Concrete*. Chicago, IL: Hanley-Wood LLC.

Piekarczyk A, Ła´zniewska-Piekarczyk B (2021) Impact of self-compacting concrete admixtures on frost resistance and compressive strength—commensurability of frost resistance criteria. *Materials* 14: Article 2922.

Safiuddin M (2003) *High performance mortar reinforced with short carbon fibers* (master's thesis). Windsor, ON: The University of Windsor.

Safiuddin M (2008) *Development of self-consolidating high performance concrete incorporating rice husk ash* (doctoral thesis). Waterloo, ON: The University of Waterloo.

Safiuddin M, Abdel-Sayed G, Hearn N (2010) *High performance mortars with short carbon fibers: properties and mix optimization*. Saarbrücken, Germany: Lambert Academic Publishing.

Safiuddin M, West JS, Soudki KA (2009) *Self-consolidating high performance concrete with rice husk ash: components, properties, and mixture design*. Saarbrücken, Germany: VDM Publishing House Ltd.

Safiuddin M, West JS, Soudki KA (2010) Flowing ability of self-consolidating concrete and its paste and mortar components incorporating rice husk ash. *Canadian Journal of Civil Engineering* 37(3): 401–412.

Safiuddin M, West JS, Soudki KA (2012) Properties of freshly mixed self-consolidating concretes incorporating rice husk ash as a supplementary cementing material. *Construction and Building Materials* 30: 833–842.

Safiuddin M, Yakhlaf M, Soudki KA (2018) Key mechanical properties and microstructure of carbon fibre reinforced self-consolidating concrete. *Construction and Building Materials* 164: 477–488.

Salam MA, Safiuddin M, Jumaat MZ (2019) Segregation resistance of self-consolidating concrete incorporating palm oil fuel ash. In *Proceedings of the 7th International Materials Specialty Conference, CSCE 2019 Annual Conference*. Laval, Quebec: Canadian Society for Civil Engineering.

Santos SA, da Silva PR, de Brito J, Evangelista L (2017) Fresh state properties of self-compacting concrete with recycled aggregate – A literature review. *Athens Journal of Technology & Engineering* 4(1): 33–46.

SCCEPG (2005) *The European guidelines for self-compacting concrete: specification, production and use*. Self-Compacting Concrete European Project Group (SCCEPG). Available at: theconcreteinitiative.eu.

Torrijos MC, Barragán BE, Zerbino RL (2008) Physical-mechanical properties, and microstructure of plain and fibre-reinforced self-compacting concrete. *Construction and Building Materials* 22(8): 1780–1788.

Yakhlaf M (2013) *Development of carbon fiber reinforced self-consolidating concrete patch for repair applications* (master's thesis). Waterloo, ON: The University of Waterloo.

Yakhlaf M, Safiuddin M, Soudki KA (2013) Properties of freshly mixed carbon fibre reinforced self-consolidating concrete. *Construction and Building Materials* 46: 224–231.

Athens Journal of Technology and Engineering - Volume 12, Issue 3, September 2025 – Pages 161-180

Survey of Historic Sims in Thailand: An In-situ, Inter-institutional Lighting Study

By Paulette Hebert & Yingsawad Chaiyakul±*

Current study was 3-day, exploratory site survey of historic Sims (small village temples used by monks) in Northeastern Thailand, conducted by team of professors/ researchers and students, hailing from universities in Thailand and USA, representing architecture and allied building disciplines. Existing conditions were documented via digital cameras. Measurements were conducted using: manual and laser tape measures. Reflected ceiling plans were developed. Light was measured using illuminance meter. Researchers compared findings to various lighting standards for various visual tasks. Luminaires and lighting techniques were noted. Sims were constructed between 1865-1953. 100% were renovated. Original illumination was natural light and candlelight. More recently, artificial sources, including fluorescent and LED were installed. Measured lighting levels exhibited variability. Some measurements did not comply with industry standards. Researchers speculated that some alterations were for practical reasons (i.e., using electric light in lieu of candles) or to reflect newer styles, (i.e. changes in height of temples) apparently to comply with new standards, over time. Researchers speculated that original candlelight produced variance with irregular flicker, creating mystery. Newer electric lighting was determined to be glaring and monotonous; mounted centrally overhead; producing relatively even light with no differentiation for important religious artifacts.

Keywords: *temple, interior, historic, Thailand, light*

Introduction

Sims are small village temples used mostly by Buddhist monks. These are often located in the rural villages of countries such as Thailand. Sims often contain a detailed and colorful mural and/or a large statue of Buddha.

In sacred buildings as well as other building types, light can illuminate interior environments, and enhance visual tasks (i.e., walking on uneven surfaces, reading from books, and viewing murals and other artwork, etc.) and can create a particular mood or ambience. Over time, however, lighting may evolve in historic structures. What was previously lit with daylight and candlelight may now be lit with modern electric replacements or supplements.

According to the Illuminating Engineering Society of North America (IESNA, also known as IES), lighting can play an important role in meeting the challenges of a building's end-users to see visual tasks and appropriate lighting can improve quality of life and promote health, well-being, and safety (DiLaura et al. 2011). In addition, the

*Professor, Oklahoma State University, USA.
±Associate Professor, Khon Kaen University, Thailand.

IES recommends that facilities view good lighting as a preventative measure and give priority consideration to facilities' lighting (DiLaura et al. 2011).

Lighting Terminology

Lighting is a complicated phenomenon and various authors and researchers have attempted to quantify and/or qualify aspects of illumination and make recommendations for lighting design. One seminal publication coined the term "compositional lighting techniques" (DiLaura et al. 2011). This speaks to the quality_of the light. The authors wrote "In lighting design, composition refers to the organization of light and color to create brightnesses that pull the various parts of the design solution into a satisfying and visually logical whole." (DiLaura et al. 2011, p. 28). These techniques include: "highlighting" (illuminating art or object 3x or more than surround), "wallwashing" (even illumination of wall), "beam play" (beam of light is predominant), "shadow play" (shadows cast by light are predominant), "silhouetting" (sandwich the object being viewed between viewer and light source resulting in no frontal detail on object), "backlighting" (illuminate through a medium, such as a translucent lens), "structural lighting" (light fixtures are mounted on beams or other structural or built-in feature), "downlighting" (lighting is aimed in downward direction), "grazing" (light source is near a textured surface and emphasizes texture, i.e. on a brick wall), "uplighting" (light is aimed in upward direction), "sparkle" (bits of brightness), "light as art" (such as if the luminaire is decorative and dominant) (DiLaura et al. 2011, 30–36).

> Another aspect of lighting is illuminance. According to ERCO (1996-2004), "Illuminance (E) may be defined as "the quantity of light incident on a surface. It is the ratio of the incident luminous flux (Φ) to the size of the surface (A). The unit of measure of illuminance is lux (lx). This is defined as lumens per square meter ($1lx = 1lm/m^2$). Illuminance recedes with the square of the distance from the light source (photometric law of distance)...The illuminance falling on a surface can be measured with an illuminance meter (in lux)" (ERCO 1996–2004).

Lighting Standards

Recognized lighting standards have been developed by various credible organizations. These include: The Illuminating Engineering Association of Thailand which produced the *TIEA Guide of Recommended Interior Illumination level (*TIEA 2016). The Illuminating Engineering Society of North America produced *The Lighting Handbook* (DiLaura et al. 2011). The Commission Internationale de l'eclairage produced *CIE Standard* (CIE 2001) and *Lighting of Indoor Work Places* (CIE 2001); and The Chartered Institution of Building Services Engineers which produced the *Code for Lighting* (CIBSE 2002). These standards have all been adopted by various municipalities or other government entities around the world and are considered to be best practices and address illuminance levels (lux, lx) that are recommended for various visual tasks.

Literature Review

Lighting in the interior environment is very important. It is especially critical when a segment of the anticipated building's end-users (DiLaura et al. 2011) (i.e., Sim temple end-users, (i.e., Buddhist monks, or villagers, visitors and tourists), tend to be older individuals). As one ages, more light (illuminance) is needed to see at the same level as a younger person (DiLaura et al. 2011). Regarding lighting and older adults, lighting design directly impacts quality of life (DiLaura et al. 2011). Older people's "quality of life experiences (are)…expressed in their perceptions, evaluations, and satisfactions…" (Campbell et al. 1976). Other researchers found a close relationship between lighting and quality of life in relation to older people and also suggested that lighting for older adults be studied and improved (Sörensen and Brunnström 1995).

Generally, prior to the current research, a dearth of published studies regarding the documentation and/or analysis of the illumination of historic, Sim building interiors, located in Thailand, was noted. A few conference presentations regarding field studies conducted in Thailand were found which examined the 1) illumination in a Catholic chapel (Hébert et al. 2017) and 2) illumination in a museum (Hébert and Chaiyakul 2020). One conference presentation (Hébert et al. 2023) examined the illumination of historic Thai Sims' interiors. However, several recent, scholarly, in-situ studies, examining existing lighting at other building types, in Australia, India, Malaysia and the USA, were found (Hébert et al. 2023, Hebert and Tanfield 2024, Stall-Meadows et al. 2011, Hébert and Erdley 2019)

Further, examinations of existing lighting at various sites in the USA, which utilized a range of measuring devices and digital tools, in-situ, including a Smart Spectrometer Data Logger, to gather empirical data, were found (Hébert and Thompsen 2011, Hébert et al. 2021, Hébert et al. 2023, Hébert et al. 2018) one published study examined the architecture of temples in Taiwan (Chen 2024). One examined the plans of Buddhist temples in Mongolia Haoribao et al. 2022). Previously, other researchers studied folk Buddhism in Taiwan in mountain temples (Mei-Rong and Quan-Zheng 2004).

Methodology

The current study consisted of three days of exploratory, site surveys during which eight different historic Sims (small village temples used mostly by monks) located in Northeastern Thailand were examined. Refer to Figure 1 for a map of where the sites are located.

Figure 1. *Map of Northeastern Thailand and Sim Site Locations*

The site survey was conducted by an international team (Americans and Thai) consisting of 18 members. The team was inter-institutional, representing four universities. Professors/researchers, undergraduate students and graduate students comprised the team. They represented architecture & allied building disciplines. Existing conditions at the Sim temple sites in Northeastern Thailand were visually documented via digital phone cameras.

Field measurements were conducted using: manual and laser tape measures: 1) Krucker manual tape measure, 2) PromaLEO250 tape measure and 3) CEM laser tape measure. Refer to Figure 2 for images of the Tape Measure Tools. These building measurements were utilized by the researchers to inform the reflected ceiling and lighting plans they created after their site visits. The reflected ceiling and lighting plans were created using AutoCAD computer-aided design software.

Figure 2. *Tape Measure Tools*

Source: Authors.

Lighting was empirically measured using an Illuminance Meter CL-500A Illuminance and industry practices. Refer to Figure 3 for a photograph of the illuminance meter.

Figure 3. *Illuminance Meter*

Source: Authors.

Light meter readings of illuminance levels were taken in the interior at each of the temples at the following locations: 1) Navigating the walkway (horizontal orientation, 0 meters (m.) above finished floor (AFF) for walking tasks), 2) Reading books (horizontal orientation, 0.50 m. AFF at "work plane height" for reading tasks and 3) Viewing mural (vertical orientation, 1.50 m. AFF). Researchers utilized descriptive statistics to determine the mean levels for their in-situ light level readings. They later compared these average levels to multiple lighting standards to check for compliance. They utilized: 1) Illuminating Engineering Association of Thailand's the *TIEA Guide of Recommended Interior Illumination level* (TIEA 2016). 2) The Illuminating Engineering Society of North America publication, *The Lighting Handbook* (DiLaura et al. 2011); 3) The Commission Internationale de l'eclairage's *CIE Standard Lighting of Indoor Work Places* (CIE 2001); and 4) The Chartered Institution of Building Services Engineers' publication entitled the *Code for Lighting* (CIBSE 2002). These aforementioned lighting standards all provided illumination recommendations regarding the quantity of light recommended for various visual tasks, (i.e., walking, reading or viewing artwork).

Researchers also identified and noted the light source types (i.e., fluorescent); luminaire types (AKA light fixtures or light fitting, i.e. open can, bare strip) and the locations of the interior luminaires (i.e., surface mounted, pendant mounted) in the Sims. They identified the associated compositional lighting techniques, utilizing Smith and Bertolone's (1986) quality of light classifications as a guide.

Figure 4. *Sim A: Chai Sri Temple, Khon Kaen*

Source: Authors.

Figure 5. *Sim B: Suan Waree Temple, Khon Kaen*

Source: Authors.

Figure 6. *Sim C: Sra Thong Temple, Khon Kaen*

Source: Authors.

Figure 7. *Sim D: Kosol Matchimawas Temple, Nakhon Phanom*

Source: Authors.

Figure 8. *Sim E: Burapharam Temple, Nakhon Phanom*

Source: Authors.

Figure 9. *Sim F: Phutthasima Temple, Nakhon Phanom*

Source: Authors.

Figure 10. *Sim G: Pa Laylai Temple, Mahasarakham*

Source: Authors.

Figure 11. *Sim H: Photharam Temple, Mahasarakham*

Source: Authors.

Figure 12. *Interior of Sim A: Chai Sri Temple, Khon Kaen*

Source: Authors.

Figure 13. *Interior of Sim B: Suan Waree Temple, Khon Kaen*

Source: Authors.

Figure 14. *Interior of Sim C: Sra Thong Temple, Khon Kaen*

Source: Authors.

Figure 15. *Interior of Sim D: Kosol Matchimawas Temple, Nakhon Phanom*

Source: Authors.

Figure 16. *Interior of Sim E: Burapharam Temple, Nakhon Phanom*

Source: Authors.

Figure 17. *Interior of Sim F: Phutthasima Temple, Nakhon Phanom*

Source: Authors.

Figure 18. *Interior of Sim G: Pa Laylai Temple, Mahasarakham*

Source: Authors.

Figure 19. *Interior of Sim H: Photharam Temple, Mahasarakham*

Source: Authors.

Findings

General

According to local records and anecdotal evidence, the eight examined Sims were originally constructed between 1865-1953. It was found that all (100%) of the Sims had been renovated over time. Observed interventions included at the sites included: 1) interior ceiling and wall repairs; 2) roof repair; 3) repairs to original interior mural paintings; 4) renovations to the volumes of Sims (i.e. raising of roofs); 4) repainting of room interiors in modern colors; 5) lighting and electrical modifications. Refer to Figures 4-19 for color photographs of the Sim sites and interiors.

Lighting

Anecdotal and some visual accretion evidence (candlewax) informed the researchers that the original illumination of the Sims had been via natural light & candlelight. More recently, artificial sources, including fluorescent and Light Emitting Diode (LED)s and associated wiring and controls (i.e., light switches), had been installed. It was found that the newer interior lighting was often mounted towards the center of Sim ceilings. Dimensioned in meters, the reflected ceiling and lighting plans of the Sim temples, showing the location of existing lighting fixtures and associated wiring observed in the current study, were developed. Refer to Figure 20-27 for the eight reflected ceiling plans. Refer to Table 1 for the Sim reflected ceiling and lighting plan legend.

Figure 20. *Reflected Ceiling Plan of Sim A: Chai Sri Temple, Khon Kaen*

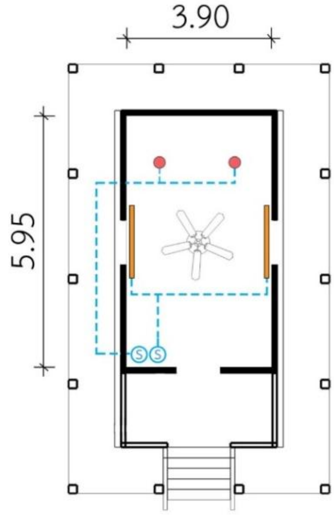

Source: Authors.

Figure 21. *Reflected Ceiling Plan of Sim B: Suan Waree Temple, Khon Kaen*

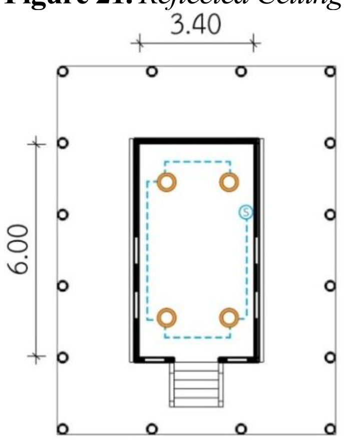

Source: Authors.

Figure 22. *Reflected Ceiling Plan of Sim C: Sra Thong Temple, Khon Kaen*

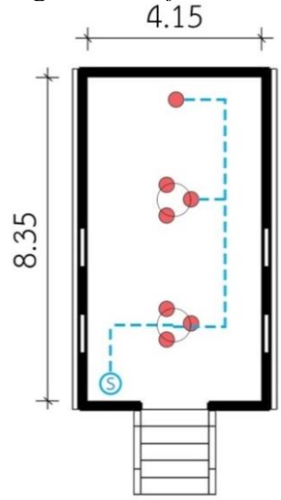

Source: Authors.

Figure 23. *Reflected Ceiling Plan of Sim D: Kosol Matchimawas Temple, Nakhon Phanom*

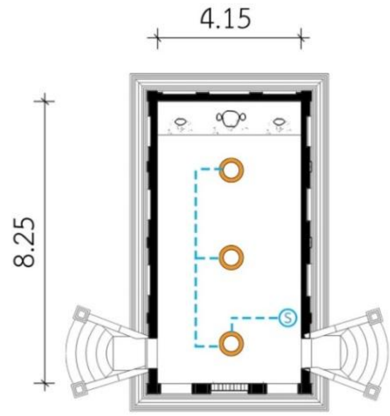

Source: Authors.

Figure 24. *Reflected Ceiling Plan of Sim E: Burapharam Temple, Nakhon Phanom*

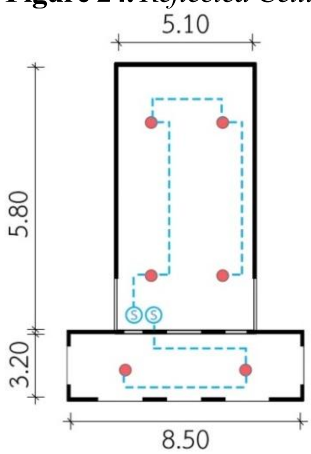

Source: Authors.

Figure 25. *Reflected Ceiling Plan of Sim F: Phutthasima Temple, Nakhon Phanom*

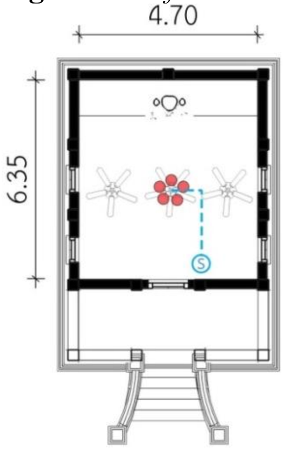

Source: Authors.

Figure 26. *Reflected Ceiling Plan of Sim G: Pa Laylai Temple, Mahasarakham*

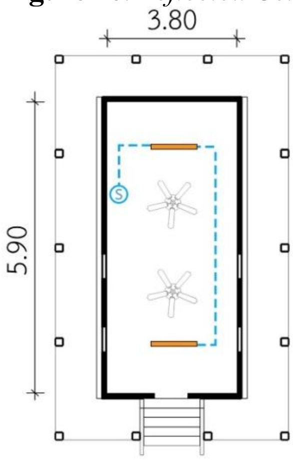

Source: Authors.

Figure 27. *Reflected Ceiling Plan of Sim H: Photharam Temple, Mahasarakham*

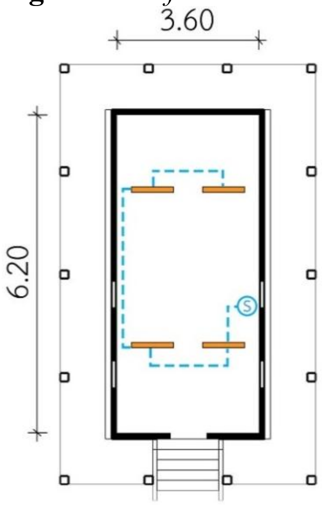

Source: Authors.

Table 1. *Sim Reflected Ceiling and Lighting Plan Legend*

Symbol	Description
	Fluorescent open can luminaire
	Fluorescent surface mounted luminaire
	Fluorescent bare strip luminaire
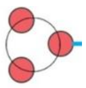	Fluorescent pendant mounted luminaire
	Ceiling fan
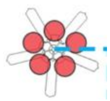	Ceiling Fan with fluorescent light kit
	Light switch

Note: Light Emitting Diode (LED) battery-operated candles had been temporarily installed at Sim D. Refer to Figure 28. These were mounted approximately one m. AFF but since they were not ceiling mounted and not electric, they were not shown in Table 1.
Source: Authors.

The researchers found that all of the newer, building-mounted, hard-wired, interior lighting consisted of fluorescent sources. Some of the fluorescents were the linear type and some were the compact type. Refer to Table 1 for the reflected ceiling and lighting plan legend which denotes light sources and mounting locations. Additionally, temporary, battery-operated, light emitting diode (LED) candles had been installed in Sim D. Refer to Figure 28 for photograph of the LED candles in Sim D.

Figure 28. *Illuminated Interior of Sim D with Temporarily Installed LED Candles*

Source: Authors.

Researchers identified the associated compositional lighting techniques, utilizing Smith and Bertolone's (1986) quality of light classifications as a guide. They determined that a total of (N=5) lighting techniques were represented within the Sims: Highlighting (n=0); Wallwashing (n=2, Sim A & C); Beam Play (n=0), Shadow Play (n=0); Silhouetting (n=0), Backlighting (n=0); Structural lighting (n=2, Sim G & H); Downlighting (n=2, Sim A & E); Grazing (n=0); Uplighting (n=0); Sparkle (n=1, Sim D); Light as Art (n=1, Sim C). Generally, there was a dearth of representation of the aforementioned compositional techniques in the examined Sims. Less than one-half (n=5, 41.6%) of the twelve compositional lighting techniques (Smith and Bertolone 1986) were found by the current researchers in the eight Sims. The illumination in the Sims was generally ambient and lacked hierarchy. Refer to Table 2 for the Compositional lighting techniques observed.

Table 2. *Compositional Lighting Techniques Observed*

	Sim Site							
	A	B	C	D	E	F	G	H
Compositional Lighting Techniques								
Highlighting								
Wallwashing	X		X					
Beam Play								
Shadow Play								
Silhouetting								
Backlighting								
Structural Lighting							X	X
Downlighting	X				X			
Grazing								
Uplighting								
Sparkle				X				
Light as Art			X					

Source: Authors.

Researchers utilized descriptive statistics to determine the mean measured illuminance levels in the eight Sims. A total of 21 mean light levels were reported. Refer to Table 3 for average illuminance levels in Sims, by task.

Table 3. *Average Illumination Levels (in lux (lx)) Measured at Specified Heights in Sims where Visual Tasks Occurred (i.e. Walking, Reading, Viewing) in Meters (m) Above Finished Floor (AFF)*

<table>
<tr><th colspan="2" rowspan="5">Sim</th><th colspan="9">Visual Task and Height of Task AFF</th></tr>
<tr><th colspan="3">Walking at 0. m.</th><th colspan="3">Reading at 0.50 m.</th><th colspan="3">Viewing Wall Mural at 1.5 m.</th></tr>
<tr><th colspan="3">Horizontal Orientation of Task & Light Meter</th><th colspan="3">Horizontal Orientation of Task & Light Meter</th><th colspan="3">Vertical Orientation of Task & Light Meter</th></tr>
<tr><th rowspan="2">Average Measured Light Level (Lux)</th><th colspan="2">Standards Recommendations</th><th rowspan="2">Average Measured Light Level (Lux)</th><th colspan="2">Standards Recommendations</th><th rowspan="2">Average Measured Light Level (Lux)</th><th colspan="2">Standards Recommendations</th></tr>
<tr><th>TIEA/ IES/ CIE</th><th>CIBSE</th><th>TIEA/ IES/ CIE</th><th>CIBSE</th><th>TIEA/ IES/ CIE</th><th>CIBSE</th></tr>
<tr><td>A</td><td>Chai Sri Temple, Khon Kaen</td><td>75**
***</td><td rowspan="8">100</td><td rowspan="8">100</td><td>88**
***</td><td rowspan="8">300</td><td rowspan="8">150</td><td>138**
***</td><td rowspan="8">300</td><td rowspan="8">150</td></tr>
<tr><td>B</td><td>Suan Waree Temple, Khon Kaen</td><td>187</td><td>229**</td><td>252**</td></tr>
<tr><td>C</td><td>Sra Thong Temple, Khon Kaen</td><td>261</td><td>205**</td><td>*</td></tr>
<tr><td>D</td><td>Kosol Matchimawas Temple, Nakhon Phanom</td><td>615</td><td>489</td><td>*</td></tr>
<tr><td>E</td><td>Burapharam Temple, Nakhon Phanom</td><td>369</td><td>386</td><td>*</td></tr>
<tr><td>F</td><td>Phutthasima Temple, Nakhon Phanom</td><td>253</td><td>219**</td><td>422</td></tr>
<tr><td>G</td><td>Pa Laylai Temple, Mahasarakham</td><td>36**
***</td><td>41**
***</td><td>69**
***</td></tr>
<tr><td>H</td><td>Photharam Temple, Mahasarakham</td><td>59**
***</td><td>59**
***</td><td>79**
***</td></tr>
</table>

Notes:
1) *No murals exist in this Sim.
2) Bolded values indicate measured light level was too low to comply with one or more standard:
TIEA/IES/CIE **
CIBSE ***
Source: Authors.

The measured interior lighting levels appeared to exhibit variability within and across the Sim temples. Average measured illuminance ranged from a low of 41 lx in Sim G to a high of 615 lx in Sim D. Some illuminance measurements did not comply with current industry standards. Refer to Table 3 for the light level measurements as compared to industry standards.

The results were compared with four standards. It was found that three of the standards (TIEA, IES and CIE) utilized the same recommended average light level for all of the visual tasks studied (walking, reading and viewing mural) and that one standard (CIBSE) was different from TIEA, IES and CIE for both of the visual tasks of *reading* and *viewing murals*. Refer to Table 3 for average measured light levels and a comparison of the measured illumination levels to the recommendations put forth in the four standards.

For the visual task of *walking* in the Sims (N=8 average measured illuminance in each of the eight Sims), it was determined that over one-third (n=3, 37.5%) of the Sims (A, G and H) did not comply with either the TIEA/IES/CIE or CIBSE standards.

For the visual task of *reading* in the Sims (N=8), it was found that almost two-thirds (n=5, 62.5%) of the average illumination levels measured in the Sims (A, B, C, F, G & H) did not comply with the TIEA/IES/CIE standards and over one-third (n=3, 37.5%) of the average illumination level in the Sims (A, G & H) did not comply with the CIBSE standard.

For the visual task of *viewing murals* (N=5), it was determined that a majority (n=4, 80%) of the average illumination levels did not comply with the TIEA/IES/ CIE standard and over one-half (n=3, 60%) did not comply with the CIBSE standard. Note that there were only five averages for the task of viewing murals because no murals existed in Sims C, D or E.

Refer to Table 3 for standards compliance.

Discussion

Researchers speculated that some of the noted renovations and interior alterations were probably made for practical reasons: (i.e., using electric light in lieu of candles to reduce fires); to reflect newer styles (i.e. changes in height and volume of temples apparently to comply with new standards, over time. The researchers speculated that originally in Sims, candlelight probably produced some variance as candle flames could be influenced by variables, (i.e. drafts and other movement within the Sims; impurities in the candle wax; moisture, wick trimming, etc.). Candlelight may flicker irregularly, presumably creating an air of mystery. Compositional technique that might be associated with candlelight include: Sparkle, Uplighting, Shadow play, Silhouette, and Highlighting. It should also be noted that historically, daylighting in Sims may have created different patterns and light levels based on time of day and changing seasons. With building alterations, some fenestration, and presumably associated daylight effects, were changed.

Generally, there was a dearth of representation of the aforementioned compositional techniques in the examined Sims. Less than one-half (n=5, 41.6%) of the twelve compositional lighting techniques, originally identified by Smith and

Bertolone (1986), were found by the current researchers in the eight Sims. The researchers perceived that the newer electric lighting in the renovated Sims was somewhat glaring, monotonous, and mostly mounted overhead in the central of the ceilings in the Sims. Unfortunately, these newer lighting installations produced relatively even illumination with no highlighting or hierarchy of light for important and sacred artifacts (i.e., mural, statue of Buddha).

Also, it should be noted that all of the examined lighting standards are relatively new and came into effect long after the Sims were originally built and potentially even after some of the Sims were renovated. The current lighting standards are based on commercially available, artificially-created, electric lighting sources (i.e., fluorescent and LED). The lighting standards generally address the needs of end-users in modern buildings within urban contexts. However, the studied Sim buildings were constructed within local contexts and originally utilized natural light and flame sources (i.e., candles) exclusively. The newer lighting standards may not take religious rituals and the intended sacred nature of the Sim interiors into account when recommending light levels for tasks such as reading. Light levels recommended for reading in an institutional setting, such as a library, and intended for longer periods of time, may need to be of higher lux than shorter readings in a temple, which may also be meant to evoke feelings of deep meaning and mystery. The applicability of the current lighting standards to this religious building type located in the rural areas of Thailand should be studied further.

Conclusions

The researchers perceived that, unfortunately, the observed building renovations appeared to not be respectful of Sims' original building typology, former ritualistic nature, and associated sacred tasks. Measured light levels varied at the examined Sims and they did not all meet the four consulted industry standards.

This research fills a gap in the literature regarding the illumination of Sim temples in Thailand and the documentation of Sims. Although only eight temples were visited, this study lays the groundwork and methodology for future Sim lighting research in Thailand and beyond.

Implications

Sims do not evoke the same spirituality with their current modifications as did the original Sims. Sims are no longer as authentic as they once were with their current modifications. The studied Sims may no longer fully support the traditional Buddhist rituals or create the same ambience as those experienced in previous times. Older end-users, including Buddhist monks, villagers, visitors and tourists, may have difficulty with some visual tasks within the Sims due to light levels and associated glare. Further, some measured light levels were far in excess of some standards' recommended light levels which could indicate an unnecessary waste of electricity.

Recommendations

Sims should be returned to original design with regards to building configurations, height and interior decoration; murals should be conserved and return to original designs; existing lighting should be replaced with the lighting better reflecting that which was originally installed with regards to: light sources, light levels, luminaire installation locations and compositional lighting techniques.

Acknowledgments

The authors are grateful for the financial support from the Faculty of Architecture, Khon Kaen University. We are also thankful to the 1st year students and academic staff from the Faculty of Industrial Technology, Sakon Nakhon Rajabhat University who joined the field study. The authors would especially like to thank Teeraphat Nongharnpitak, Hanny Chandra Pratama and Supachock Sonthichai from Suan Sunandha Rajabhat University for their work on data collection. Chumnan Boonyaputthipong is also gratefully acknowledged for data collection participation and other research contributions. We also wish to thank Don and Cathey Humphreys.

References

Campbell A, Converse PE, Rodgers WL (1976) *The quality of American life: Perceptions, evaluations, and satisfactions*. Russell Sage Foundation.

Chartered Institution of Building Services Engineers, Society of Light and Lighting (2002) *Code for Lighting*. Routledge.

Chen Y-B (2024) In-between Institutional Religion and Folk Faith during the Transition into a Modern Political System–The Case of Giam Temples in Taiwan. *Athens Journal of Architecture* 10(1): 55–85.

Commission Internationale de l'eclairage (CIE) (2001) *CIE Standard Lighting of Indoor Workplaces*. Vienna, CIE Central Bureau.

DiLaura D, Houser K, Mistrick R, Steffy (2011) *ESNA Lighting Handbook 10th edition*. Illumination Engineering Society of North America.

ERCO (n.d.) *ERCO News: Illuminance: definition, measurement and calculation*. Available at: https://www.erco.com/en_us/designing-with-light/lighting-knowledge/photometry/illuminance-7517/.

Haoribao E, Natsume Y, Hamada S (2022) Arrangement Plan of Inner Mongolia Buddhist Temple. *Athens Journal of Architecture* 8(1): 67–90.

Hébert PR, Barta S, Singh C, Esmaeili M, Jackson M, Korneva K (2023) Building Renovation Design Partnership with Non-Profit Agency: Documenting the Programming Phase of a Graduate Student Team's Design Project. *Journal of Building Energy and Environment* 5(2): 32–48.

Hébert PR, Chaiyakul Y (2020) Case study of exhibit illumination in a Buddhist monks' museum in Thailand. In *Mountains-Plains Museum Association (MPMA) Conference*, Online, September 29-October 2.

Hébert PR, Chaiyakul Y, Aruni N, Jaruphongtawit R, Tongpong N, Chandrasekera T (2017) Evaluating illumination at an art and culture museum in Thailand targeted for patrons across the life course: Recent Fulbright project spurs U.S. & Thai architecture and design Programs' international collaboration. In *Mountains-Plains Museum Association Conference*, Denver, CO, October 15-19.

Hébert PR, Chaiyakul Y, Aruni N, Kang M, Clare G, Peek G (2017) Considering the Quality and Quantity of Lighting in an Older Adult Congregate Facility Chapel in Northeastern Thailand: An In Situ Study. In *EDRA4 Proceedings*.

Hébert PR, Chaiyakul Y, Aruni N, Roberts E, Kang M, Clare G (2017) Interdisciplinary, inter-institutional Fulbright project in Thailand: Considering how light and room finishes may affect older adults' worship in a Catholic chapel. In *38th Annual Meeting of the Southern Gerontological Society (SGS)*, Asheville, North Carolina, April 6-9.

Hébert PR, Chaiyakul Y, Nongharnpitakand T, Chandra Pratama H, Sonthichai S, Clare G (2023) Survey of Historic Sims in Thailand: An In-situ, Inter-institutional Lighting Study. In *17th Annual International Conference on Global Studies: Business, Economic, Political, Social and Cultural Aspects*, Athens, Greece, (Juried), December 18-21.

Hébert PR, Clare G Singh C, VanDusen A, Hamlett C (2021) Considering industrial lighting levels in-situ in Northern India: A Textile factory study. In *Health Disparities Conference*, Online, April 7-8, 2021.

Hébert PR, Erdley M (2019) Malaysian cultural museum illumination: Special considerations for artifact preservation across patrons' life courses. In *Mountains-Plains Museum Association Conference*, Albuquerque, New Mexico, September 22-25.

Hébert PR, Jayadas A, Wright J, Losh P (2023) Existing lighting conditions in a clinic: In-Situ case study and comparison to standards. In *Health Disparities Conference*, New Orleans, LA, (Juried), February 22-24.

Hébert PR, Kang M, Singh C (2021) Considering the Illumination of a University Library Browsing Room: A Case Study of Existing Conditions and Retrofit Recommendations. *Journal of Building Energy and Environment* 5(5): 12–30.

Hébert PR, Petrova A, Clare G, Pei Y (2018) Exploring New Light and Color Instruments for Multidisciplinary Students' Use: Empirical Properties of Existing Building Illumination and the Effects of Light on Color Samples. *Journal of Building Energy and Environment* 1(1): 5–16.

Hébert PR, Tanfield K (2024) Considering Luminance & Glare In-Situ Properties Frequented by Ageing Population. In *The 30th Pacific Rim Real Estate Society Annual Conference*. Gold Coast, Queensland, Australia, (Juried), January 14-17.

Hébert PR, Thompsen R (2011) An investigation of residential display cases: Illumination protecting fragile artifacts in situ. In *Housing and Education Research Association Proceedings*, 15–19.

Illuminating Engineering Association of Thailand – TIEA (2016) TIEA-GD003(WD): TIEA *Guide of Recommended Interior Illumination level*. Bangkok: TIEA.

Illuminating Engineering Society – IES (2007) *Lighting and the visual environment for senior living*. ANSI/IESNA RP-28-07. NYC: IES.

Mei-Rong L, Quan-Zheng S (2004) The Tradition of Folk Buddhism in Taiwan as Revealed in the Kuan-yin Belief in Giam-a (Mountain Temples) and its Social Practice. *New Century Religious Study* 2(3): 1–34.

Smith FK, Bertolone FJ, Hines DC (1986) *Bringing interiors to light: The principles and practices of lighting design*. Lakewood: Whitney Library of Design.

Sörensen S, Brunnström G (1995) Quality of light and quality of life: An intervention study among older people. *International Journal of Lighting Research and Technology* 27(2): 113–118.

Athens Journal of Technology and Engineering - Volume 12, Issue 3,
September 2025 – Pages 181-194

Hybrid 3D Metal Printing Process Optimization using ML and AI

By Pavel Ikonomov[*]

Metal additive manufacturing (AM), or 3D printing, typically builds parts layer-by-layer using an additive process. However, many AM techniques often require support structures, and the final parts may not meet the required dimensional accuracy or surface finish directly from the printer. This process necessitates a separate subtractive process, such as CNC machining, to achieve the desired quality. Our innovative hybrid metal 3d printing technology addresses these limitations by combining additive and subtractive processes within a single machine. This technology eliminates the need for separate machines and post-processing steps, streamlining production and reducing overall lead times. 3D Hybrid metal printer developed at Western Michigan University combines two manufacturing methods - additive manufacturing and Computer Numeric Control (CNC) machining. The additive process uses the gas metal arc welding (GMAW) method to deposit each metal layer along a path controlled with CNC. The subtractive machining process is performed on the same CNC-controlled machine. The 3D Hybrid metal printer iterates between these two processes, adding material with welding and then using CNC machining to refine the surface. These additive/ subtractive processes are repeated until the final 3D object is complete to achieve the essential geometrical and quality requirements, the same as machining with a typical CNC machine. Traditional manufacturing processes have been refined for many years to guarantee defect-free parts, while 3D printing often requires manual intervention and might produce imperfect layers. To address these issues, we developed an automated 3D metal printing process using sensors for feedback during the printing process and machine learning/artificial intelligence (ML/AI) algorithms to optimize the printing. This process aims to reduce costs, printing time, and waste while achieving first-time printing success with the same quality as traditional methods.

Keywords: *hybrid metal 3D Printing, additive manufacturing, cnc machining, machine Learning, Artificial Intelligence*

Introduction

Traditional metal manufacturing processes, honed over many years, excel at producing high-quality parts with reliable internal structures. 3D printing provides numerous advantages over traditional methods like complex geometrical designs, on-demand manufacturing, new materials, and reduced material usage. Additive Manufacturing (AM), also known as 3D printing, has traditionally focused on creating components from thermoplastics. However, the technology is rapidly evolving to encompass metal 3D printing, enabling the production of complex metal parts that have the functionality of products made with traditional technologies.

[*]Professor, Western Michigan University, USA.

Several AM methods, including metal powder, wire, filament, and different fusion techniques, are commonly used for producing 3D metal parts. Each technique offers unique advantages and limitations, producing metal parts of varying quality, size, cost, and mechanical properties. However, challenges like slow printing speed and inconsistent material structure prevent broader adoption in the industry.

Existing AM technology

There are four general types of AM metal printing methods: Metal Powder Bed Fusion (MBF), Metal Binder Jetting (MBJ), Direct Energy Deposition (DED), and Metal Material Extrusion (MME) (Simpson 2024).

The first method, metal powder bed fusion (MBF), encompasses three key technologies: direct metal laser sintering (DMLS), selective laser melting (SLM), and electron beam melting (EBM). DMLS/SML works by spreading a thin layer of metallic powder on a platform. Then, a high-powered laser beam precisely melts or sinters the desired pattern within the powder, fusing the particles together. This process is repeated, building the part one layer at a time. SLM uses a single metal powder, while DMLS can combine different metal powders. EBM utilizes a high-powered electron beam to melt the metal instead of a laser. This allows EBM to handle refractory and reactive metal alloys that might be challenging for lasers due to their high melting points or reactive nature (Wohlers Report 2022). MBF's advantage is that it offers 3D printing of complex metal parts with properties comparable to wrought metals. Disadvantages include the need for specialized support, post-processing steps are often necessary, and build sizes need to be improved. Additionally, the cost of equipment and materials can be high (Metal 3D Printing 2024).

The second method, metal binder jetting (MBJ), an inkjet-based process, is a 3D printing technology pioneered at MIT in the 1990s. MBJ utilizes a layer-by-layer process. Here, a thin layer of metal powder is spread, followed by an inkjet head that sprays a binding agent to adhering particles. Rebinding and sintering in a furnace are essential to producing solid parts. MBJ boasts several advantages: it produces large parts with high-speed printing without supporting structures and is cost-effective due to lower material waste and potentially faster printing times. Disadvantages include lower resolution and lower mechanical properties than other metal 3D printing technologies.

The third method, direct energy deposition (DED), has two sub-types: laser-engineered net shaping (LENS) and direct metal deposition (DMD). This method offers a versatile metal 3D printing method similar to welding. It works similarly to welding by melting metal powder or wire using a laser, electron beam, or arc onto a metal substrate, building parts layer-by-layer (Wohlers Report 2022). DED excels in producing large parts with efficient material usage and fast printing speeds. Additionally, it can achieve solid metal with good mechanical properties, especially when using inexpensive metal wire. However, DED has limitations. Due to lower surface quality and detail resolution, the process often requires post-processing, such as machining. Support structures are also usually necessary, and DED can involve expensive equipment and operation costs.

Metal Material Extrusion (MME), the fourth method, also called Bound powder deposition (BPD), a recent addition to the metal 3D printing technology, borrows principles from Fused Deposition Modeling (FDM) used for plastics. MME utilizes filaments, pellets, or rods containing metal powder to build parts layer-by-layer. Like Binder Jetting, these parts require debinding and sintering in a furnace to achieve final strength. While offering the advantage of being the most cost-effective metal 3D printing method with user-friendly operation, MME has limitations. The resulting parts often exhibit higher porosity and lower mechanical properties than other methods. Additionally, debinding and sintering add complexity, and the process can be susceptible to precision and geometry imperfections caused by shrinkage during sintering (Metal 3D Printing 2024; Simpson 2024).

Current 3D metal printing technologies face limitations, including inconsistent material structures, the need for specialized chambers, and high overall costs encompassing purchase, installation, operation, and maintenance. Additionally, most methods rely on support structures, adding complexity and requiring post-processing to remove excess material and achieve desired tolerances and surface finish. These challenges highlight the need for a more streamlined, cost-effective, and user-friendly approach to 3D metal printing.

Hybrid 3D Metal Printing for Complete Metal Products

Hybrid manufacturing applies additive and subtractive (machining) processes sequentially on the same machine. There are several technologies utilizing hybrid 3D metal printing.

Hybrid Manufacturing Technologies (HMT) is using AMBIT™ integration to control the AM; a laser melts the metal wire for deposition and the subtractive CNC machining (Hybrid Manufacturing 2024).

DMG Mori applies similar laser metal deposition technology with 5-axis machining capabilities. Matsuura's LUMEX hybrid integrates AM metal powder bed fusion (SLM) with CNC milling. Optomec's LENS systems utilize an AM high-powered electron beam for DED, and some LENS integrate it with milling (Kauppila 2024).

Researchers at Western Michigan University (WMU) have developed and patented an advanced hybrid 3D metal printing process that merges additive and subtractive manufacturing techniques (US Patent 10,688,581 2020). This innovative method combines the layer-by-layer approach of additive Gas Metal Arc Welding (GMAW) welding with the precise machining capabilities of CNC machines. This unique combination allows for the creation of 3D components using a wide range of metals and metal alloys. The machine's CNC-controlled 5-axis motion (3 linear and two rotational) ensures precise control throughout the entire process, from initial material deposition to final machining (see Figure 1). First, an automatic welding arm, guided by the CNC controller, deposits metal following a predefined computer-controlled path for each layer. This process is followed by the CNC machining tool, which removes excess material to achieve the desired final shape and quality, delivering complete, ready-to-use functional parts.

Figure 1. *Stages of Hybrid 3D Printing-MIG Welding Deposition and CNC Machining of Overhang Structure*

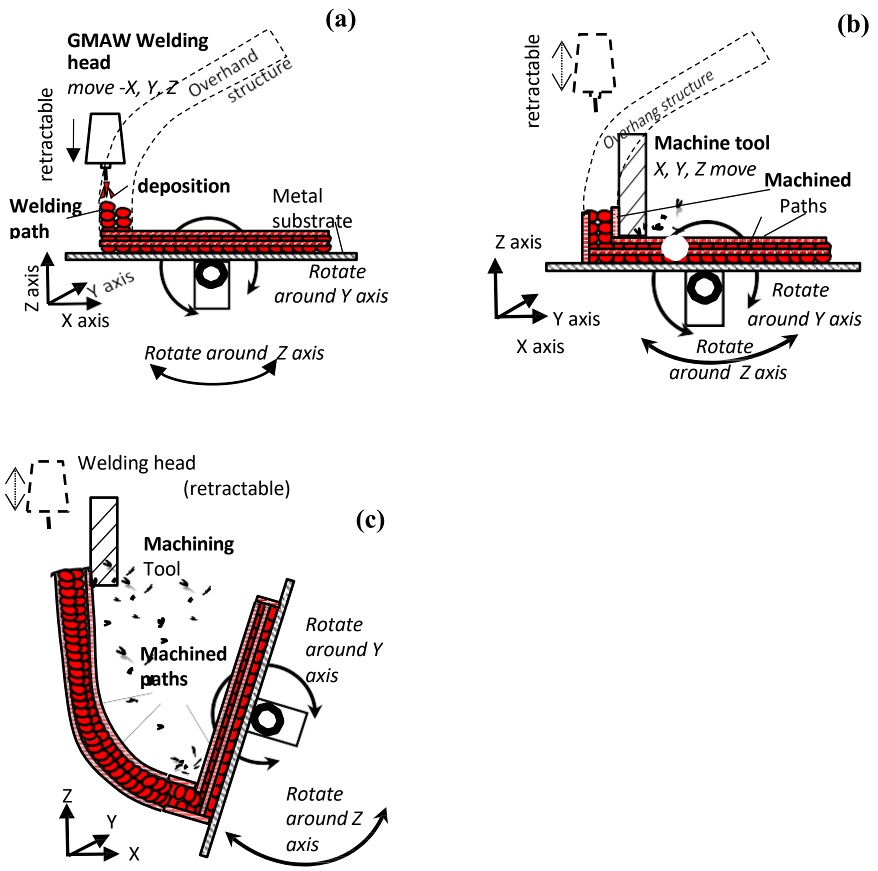

Our advanced hybrid technology integrates additive and subtractive processes within each layer of the 3D printing process, enabling single-machine product completion. While this one-stop solution offers significant advantages, it presents unique challenges in developing smart software for fully automated, unattended operations. Our team is tackling this by creating software and hardware solutions to analyze data from the 3D printer. This data will fuel the development of AI/ML algorithms for optimizing and fine-tuning the printing process, ensuring consistent, high-quality products layer-by-layer right from the first print. This automated system will leverage AI/ML software for real-time visual inspection and correction, aiming to eliminate the need for manual intervention in setting up machine parameters, quality control, and adjustments.

Our novel hybrid 3D metal printing technology is now operational. It has successfully produced validated parts for multiple industry partners (Flexco Co., Ausco Co., Forest River Co., and others).

The automated hybrid 3D metal printing solution goes beyond the machine itself. The complete package includes a computerized control system seamlessly integrated with the CNC and welding controllers, optimizing both additive and subtractive processes. A 3D metal part process optimizer also tackles efficiency by suggesting an optimal part layout on the printing plate. Finally, an in-process quality inspection system utilizes optical/laser 3D scanning and image processing for automatic alignment, tuning, and part inspection. This system ensures quality control throughout the printing process, verifying both dimensional accuracy and the surface finish of the final product. Furthermore, AI/ML-powered automation has the potential to be adapted to other 3D printing processes.

Methodology

The processes behind hybrid 3D printing are significantly different from traditional casting, welding, and machining manufacturing methods. This novel technology creates new possibilities for part design and production. However, further study is needed to fully understand hybrid printing's capabilities. A crucial aspect of this research involves ensuring that the 3D-printed parts meet industry standards for material structure and quality of the finished product (Additive Manufacturing Standards 2024).

Some problems in 3D metal printing structures are caused by the thermal stresses from the metal deposition process. Each layer experiences intense heating and cooling, leading to the formation of tiny defects like pores and cracks within the layers, compromising the part's mechanical properties. When the subsequent layers are deposited on top of cooling ones, residual stress accumulates, potentially causing cracks between layers and warping the surface. Additionally, some other defects may remain hidden within the internal structure and, depending on the printing parameters used, can exhibit anisotropic properties. To ensure the structural integrity of 3D printed metal parts, robust control processes are essential to minimize or eliminate these internal defects (Chua 2017, Clifford 2001).

Testing Isotopy of the Metal deposited in different Deposition Directions

One significant consequence of 3D printing's layer-by-layer nature is anisotropy. Typically, layers exhibit isotropic properties in the XY plane due to the material deposition process. However, properties in the Z direction (perpendicular to the layers) are often weaker. Delivery path directions, the width, and the layer thickness can also influence these variations. We tested the sample material's properties when deposited along the X-axis, in a crosshatch pattern along the Y-axis, at a 45-degree angle from the X-axis, and vertically along the Z-axis.

Optimization of the Deposition Path

Initial printing tests revealed challenges at the start and end of each deposition layer due to the nature of the welding process. A bump was formed at the beginning of the deposition, and a material drop was observed at the end of a layer, where the molten metal pool spilled upon the termination of the electric arc, leading to insufficient material deposit—this inconsistency deposition to the following layers creating distorted structure. Furthermore, when several layers are printed on each other, the split overflow expands on the sides, increasing the amount of material needed for print and removal.

To address the initial challenge of the material fluctuation at the start and end of each deposition layer, we explored forward and reverse-directional printing strategies.

Figure 2. *Deposition on "Z" Direction and Forward Reverse Directional Printing*

This successful approach allowed us to achieve significant build heights exceeding 8 inches (203.2 mm) on the Z-axis, see Figure 2.

Figure 3. *Deposition on "X" Direction with Side Step*

Figure 4. *"Z" Pattern Deposition*

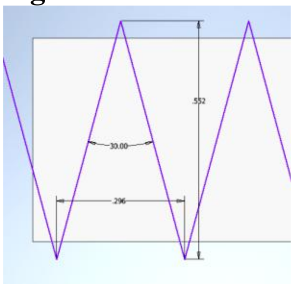

Figure 5. *Part with "Z" Pattern Deposition*

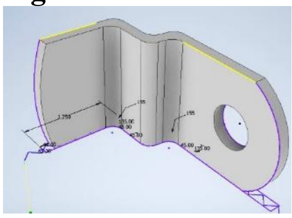

Another challenge we encountered involved inconsistencies in the side overlap line path between layers lines on the XY plane. While increasing the overlap parameter addressed this initially, it led to a new issue: variations in layer height or material overflow if the lines were placed too close or apart (see Figure 3).

To solve the problems described above, we consulted with industrial partners to discover how they could resolve similar issues. Based on those findings, we created the so-called zig-zag ("Z") welding pattern (see Figures 4 and 5).

This pattern demonstrated its effectiveness in achieving maximum uniformity in both the height and width of the deposited material. During testing, we discovered that the success of the "Z" pattern relies on careful optimization of key parameters: overall pattern width, directional change angle, and the CNC machine's feed rate, see Figure 6.

Figure 6. *Testing "Z" Pattern Path Paraments*

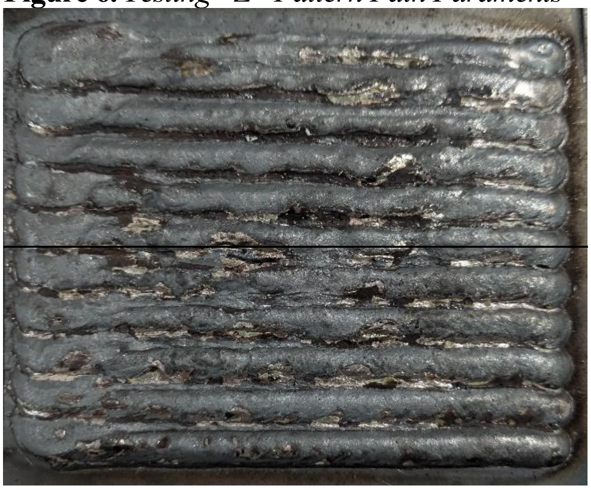

Testing Results

To ensure our hybrid 3D metal printer produces high-quality parts, samples undergo rigorous destructive and non-destructive testing (Technical Specification Sheet ER70S-6 2020), which is performed additionally to meet dimensional and tolerance specifications.

Destructive Testing

Our optimized hybrid 3D printing and CNC machining process has successfully eliminated porosity, cracks, and material imperfections in all tested samples. These samples were produced using various deposition directions, including X and Y axes, 45 degrees, and horizontally and vertically along the Z-axis. While most samples utilized linear deposition, some stainless-steel samples employed a novel "Z" pattern for deposition. This successful outcome across diverse deposition methods demonstrates the effectiveness of our optimized process.

Tensile testing: Tensile testing, conducted according to (ASTM A36 2024, Chua 2017), evaluated the strength of samples produced using various material deposition directions (X, Y, Z, 45° degrees, and vertical side). Over 250 sub-sized specimens (100x6x6 mm) were tested. The results, shown in Figure 7, demonstrate notable consistency across all directions, with an average yield strength and ultimate tensile strength of 395 MPa and 500 MPa, respectively.

Figure 7. *Tensile Testing X, Y, Z, 45° Degrees and Side Directions of Material Delivery*

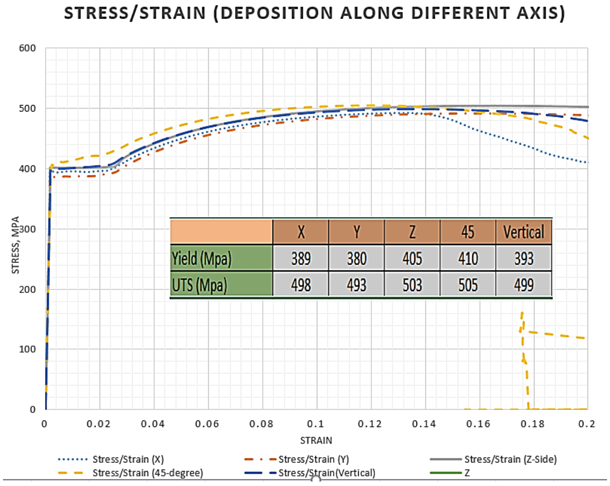

Our 3D-printed parts achieved impressive tensile properties. Compared to the reference materials, ER70S-6 Gas Metal Arc Welding (GMAW) wire, which has an ultimate tensile strength of 586 MPa and yield strength of 483 MPa (Welding test 2024), our printed parts exhibit comparable or even exceeding values. Furthermore, ASTM A36 mild/low carbon steel, known for its strength between 380 MPa and 505 MPa in yield and ultimate tensile strength (Baldev 2002), falls below the average performance of our 3D printed samples.

Bend tests: Bend testing exhibits equivalent or superior bending properties compared to ASTM A36 mild/low carbon steel (ASTM36 2024).

Hardness testing: Our 3D printed samples (average Brinell 173, hardeners Rockwell B 94.8, hardeners Rockwell C 65, have identical or better hardness properties than GMAW welding wire MDS specifications and higher than ASTM A36 mild/low carbon steel (Moreno 2013).

Rigorous testing demonstrates that our technology delivers exceptional isotropy, meaning the mechanical properties of the printed parts remain consistent across all directions (X, Y, and Z axes). This achievement eliminates concerns about anisotropic properties, a common challenge in 3D printing, and ensures the parts perform uniformly regardless of the force applied.

Nondestructive Testing

Liquid penetrant testing, a standard method for detecting welding cracks or pores, was performed using Cantesco D101-A developer and Cantesco P301W-A dye. This inspection revealed no presence of cracks or pores on the material surface, further solidifying the high quality of our 3D printed parts.

Metallurgical Testing

We conducted a thorough metallurgical microstructure analysis of grain boundary cleanliness, porosity, and the absence of fusion defects/cracks to validate the quality of our hybrid 3D printing process. Samples were sectioned in three orthogonal planes (XY, YZ, and XZ) for each printing direction (X, Y, Z, and 45 degrees).

Optical microscopes: First, the microstructure testing was performed using Nikon optical microscope magnifications of x400 and x1,000, and no porosity, cracks, or other imperfections were found.

Further analysis using a Keyence MicroscopeVR-3000 with 1 µm resolution and a new digital Keynce Microscope VHX-7000 series with magnification up to 6000 times and a resolution of 0.5 meticulously evaluated the 3D surface imperfections of the samples. We measured roughness, flatness, form, contour deviations, and various 3D parameters like height differences, area, volume, and roughness. Consistent with the previous tests, no pores or cracks were detected on any sample. The surface roughness, 0.57 µm, of the hybrid process was the same as that of the standard CNC milling process.

CT X-ray scans: CT X-ray scans were performed on several parts before being delivered to the user. They show no defects such as cracks, cavities, or porosity; see Figure 8 for details.

Figure 8. *CT X-Ray Scans of Parts #1 and #2 Produced for Industry*

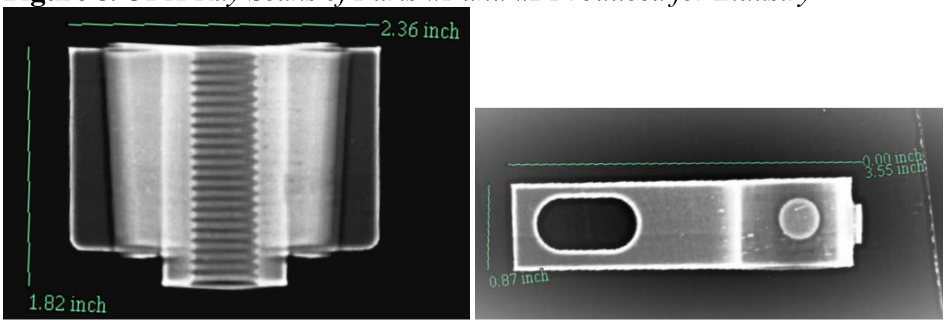

Extensive testing proved that the printed parts exhibit isotropic mechanical and quality properties. This achievement overcomes a significant hurdle in traditional 3D printing. Furthermore, rigorous inspections confirmed superior internal and external structures, free from defects like cracks or pores. Finally, surface quality analysis revealed a roughness comparable to standard CNC milling processes. These combined results validate the effectiveness of our technology in producing high-quality metal parts with excellent properties.

Testing of the Automated Hybrid 3D Printing System

Automated Hybrid 3D Printing System with Feedback from 3D Scanner

The 3D hybrid metal printer's success hinges on each layer's precise and uniform deposition. Initially, this process relied solely on the operator's visual judgment to identify and correct layer inconsistencies. However, human observation has inherent limitations in achieving the high accuracy required for each layer. To address this challenge, we developed an automated feedback measuring system, significantly enhancing the precision and consistency of our printing process.

At first, we measured the height of points on a layer with a touch CNC 3D probe, which works similarly to a Coordinate Measuring Machine (CMM). This electromechanical measurement method is standard in CNC machining manufacturing.

However, the ball-end touch probe's single-point measurement capability introduces subjectivity and potential for error due to the manual operator's positioning and settings, and it is a slow process.

Recognizing the limitations of single-point measurements and the time constraints associated with the ball-end probe, we implemented a red light laser profile scanner, the Gocator 2330A from LMI Technologies, to significantly enhance the accuracy and automation of layer 3D measurements. The scanner, attached to the CNC's automatic tool changer, captures micron-level 3D profiles of each layer. The Gocator boasts an internal processing unit for real-time measurements, which we integrated with the CNC controller. Extensive programming efforts were undertaken to integrate the additive manufacturing process seamlessly with this new scanning feedback system.

We tested the scanner's performance with an example of an insufficient material layer during the additive process (see Figure 9).

Figure 9. *Testing of Intentional Insufficient Additive Deposition*

This measurement allowed us to develop and rigorously test patch subroutines that utilize 3D scanning and positioning feedback. These subroutines address deficiencies in both the Z-axis (height) and X-axis (width) directions, see Figure 10.

Figure 10. *Additive Layer Patch Results*

The 3D Hybrid Metal Printer's capabilities were successfully demonstrated through a collaborative project with Forest River Inc., for which various components were printed and tested. This project was a valuable platform for developing and recording optimal printing techniques. The in-process feedback and correction system is critical in ensuring repeatability and successfully printing metal components.

Preprocess and Real-Time Automation

Preprocess Optimization Using ML/AI

Our research involved producing and measuring hundreds of 3D metal samples to optimize printing parameters for various materials. Currently, an offline system analyzes these samples using image processing, a touch probe, and 3D scanning measurements. This comprehensive approach has allowed us to optimize parameters for mild steel, hard steel, stainless steel, and aluminum used in our hybrid 3D printing process.

The optimized parameters are then implemented within the CNC and GMAW equipment controllers (see Table 1). For CNC control, these include the feed rate (table movement speed) and deposition head height for each layer. GMAW control parameters encompass wire feed speed, power (voltage/amperage), nozzle offset, and pulse control. Importantly, parameter optimization focuses on identifying bordered values that ensure successful material deposition, excluding cases with insufficient material from further consideration.

Machine learning algorithms, including multi-parameter linear regression, split-sample validation, K-fold cross-validation, and backpropagation neural networks, were important steps in optimizing the 3D printing parameters for various materials and automating the processes.

Table 1. *Parameters and Measured Values (Partial List)*

Plate#; Layer#	Machine Feed speed, in/min	Welding Wire Feed Speed, in./min	Trim-Power A/V	Height Weld gun, mm	Height-MAX-mm	Height-Min-mm	Width-MAX-mm	Width-Min-mm
Plate-7; Layer-1	20	285	1.15	25.400	3.48	2.57	7.33	5.30
Plate-7; Layer-2	20	285	1.15	22.225	3.59	2.53	7.10	5.40
Plate-7; Layer-3	20	285	1.15	19.150	3.59	2.80	6.96	5.42
Plate-7; Layer-4	20	285	1.15	15.875	3.53	2.32	6.99	6.04
Continue….								

Our ongoing research efforts are focused on developing a real-time, in-situ feedback system that leverages machine learning and AI optimization for even greater optimization. A significant advantage of our system is its expandability to other materials as long as they are compatible with GMAW (MIG) welding. This opens doors for future exploration and broader material adoption within our hybrid 3D printing process.

Real-Time AI/ML Automation

We are in the process of implementing an automated system using real-time measurements and feedback that works without human intervention. It employs a multi-camera setup that captures images from various angles for processing. These images are then analyzed by dedicated computers using machine learning (ML) and artificial intelligence (AI) algorithms, with the results being fed back to the 3D metal printing system.

This process will be further optimized and accelerated by designing and building a specialized computer that enables real-time data processing and optimization at a millisecond scale. This automation of image processing and measurements will provide instant feedback to the system, allowing for precise parameter adjustment during each layer deposition. Additionally, the system integrates with automatic 3D scanning, facilitating in-process measurement and parameter correction for 3D printing and CNC machining. Our system goal is to transform the automation of real-time quality control in 3D metal printing to create a perfect product without human intervention.

Conclusion

We have been developing and testing a high-performance Hybrid 3D Metal Printer that leverages Artificial Intelligence (AI) and Machine Learning (ML) for process optimization. This innovative approach optimizes additive and subtractive processes, paving the way for a fully integrated 3D printer with an in-situ control system. The system comprises custom software and hardware, including sensors for image and 3D laser scan data acquisition. This comprehensive data collection allows our AI/ML algorithms to perform real-time optimization and tuning, ensuring consistent, layer-by-layer quality and accuracy without manual intervention. Extensive testing has been conducted, involving creating hundreds of samples for parameter optimization and delivering multiple finished parts to collaborating companies for equipment compatibility testing. The successful completion of these rigorous tests confirms that our Hybrid 3D printing process meets stringent industrial standards and requirements.

References

Additive Manufacturing Standards (2024) https://www.astm.org/products-services/standards - and-publications/standards/additive-manufacturing-standards.html?form=MG0AV3.

ASTM A36 (2024) *Mild/Low Carbon Steel*. https://www.azom.com/article.aspx?ArticleID= 6117.

Chua CK, Wong CH, Yeong WY (2017) *Standards, Quality Control, and Measurement Sciences in 3D Printing and Additive Manufacturing.* Elsevier Ltd.

Hybrid Manufacturing Technologies (2024) https://hybridmanutech.com/portfolio/ambit_multi/.

Kauppila I (2024) *3D Printing & CNC: A Guide to the Best Hybrid 3D Printers*. https://all3 dp.com/1/3d-printing-cnc-guide-to-hybrid-additive-subtractive-manufacturing/.

Matthews C (2001) *ASME engineer's data book*. ASME Press.

Metal 3D Printing (2024) *An Overview of the Most Common Types*. https://3dprinting.com/ metal/types-of-metal-3d-printing/.

Moreno P (2013) *Welding Defects.* 1st Edition. Aracne.

Raj B, Jayakumar T, Thavasimuthu M (2002) *Practical non-destructive testing.* 2nd Edition. Woodhead Publishing.

Simpson TW (2024) *Material Extrusion: Now with Metal*. https://www.additivemanufactu ring.media/blog/post/material-extrusion-now-with-metal.

US Patent 10,688,581 (2020) Jim Mcqueen, Daniel Ziemer, Matt Ziemer, Jake Ives, Pavel Ikonomov. *3D Metal Printing Device and Process, US patent: US I20170144242 A1*.

Welding Test (2024) https://www.angelfire.com/my/welding/test.html.

Wohlers Report (2022) *3D printing industry and additive manufacturing*. https://wohlersas sociates.com/product/wohlers-report-2022/.

Athens Journal of Technology and Engineering - Volume 12, Issue 3, September 2025 – Pages 195-210

Internal Model Principle-based Control for Sinusoidal Disturbance Rejection in Field-Oriented Control

By Ibrahim Allafi[*] & Lyndon Brown[±]

This research presents results of combining the field-oriented control of motors with a more general Internal Model Principle controller rather than the specific case of integral control. The goal is to have a motor that can remove narrow band disturbances without impacting its performance outside of this specific frequency. This research is motivated by eliminating tremors in human limbs. We verify our approach by initially implementing the algorithm in Matlab and then conducting experimental trials in our lab using two brushless DC motors. The first motor (Motor 1) will generate a sinusoidal torque signal on the shaft, while the second motor (Motor 2) will utilize our algorithm to cancel this torque. Both motors are connected by a coupler. When Motor 1 initiates rotation with a sinusoidal torque signal, Motor 2 driven with our algorithm will freeze the motion in Motor 1. Thus, the torque on Motor 2 will match that of Motor 1. We then add additional broadband torque in Motor 1 and show that Motor 2 can still match the sinusoidal torque while ignoring this additional movement. We will investigate the difference between using the encoders from both motors as the driving signal for our control algorithm.

Keywords: *internal model principle, field-Oriented Control, disturbance rejection, brushless DC motors, tremor signal*

Introduction

The challenge of disturbance cancellation arises in numerous applications, such as active noise and vibration control, optical stabilization in laser communication systems, vibration management in space structures due to control moment gyroscopes, helicopter vibration reduction, and tension regulation in paper machines (Pigg & Bodson 2009). Rotating mechanical systems like magnetic disk drives (Brown & Zhang 2004) and CD players often experience periodic disturbances (Pigg & Bodson 2011).

Two methods are suggested for rejecting sinusoidal disturbances. The first method is an indirect approach, where the frequency of the disturbance is estimated, and then the control law's magnitude and phase are adjusted accordingly based on this estimated frequency. The second method is a direct approach, which simultaneously estimates and cancels the disturbance frequency using a phase-locked loop (Bodson & Douglas 1997). Brown and Zhang (2004) introduce an algorithm designed to eliminate periodic disturbances with uncertain frequencies. This algorithm employs an internal model structure with an adaptive frequency component, which operates

[*]PhD Student, Western University, Canada.
[±]Associate Professor, Western University, Canada.

alongside a stabilizing controller. In Pigg and Bodson (2009), the challenge of disturbance rejection is addressed for plants with unknown and time-varying characteristics. The algorithm by Pigg and Bodson (2009) utilizes online estimates of the plant's frequency response and disturbance parameters to tackle this issue. Pigg and Bodson (2013) suggest an algorithm that relies on an adaptive harmonic steady-state and a magnitude phase-locked loop to cancel disturbances of uncertain frequencies affecting an unknown plant. On the other hand, Pigg and Bodson (2011) introduced a novel algorithm for estimating frequencies using a two-phase induction motor model, effectively rejecting disturbances of unknown frequencies.

Recent progress in disturbance rejection methods has introduced new strategies to handle sinusoidal disturbances in mechanical systems. Kamaldar and Hoagg (2021) presented adaptive harmonic control algorithms, both centralized and decentralized, which use discrete Fourier transform data to counteract known-frequency sinusoidal disturbances in systems with multiple inputs and outputs. Wen and Yan (2020) proposed a control method based on disturbance prediction, using an additional observer to forecast and reject unknown sinusoidal disturbances, improving the stability of systems with time delays. R. Madonski and colleagues (2020) developed a robust control algorithm within the active disturbance rejection control framework, including a tool to estimate harmonic disturbance frequencies, and showed its effectiveness through tests on torsional systems. Lastly, Long (2021) investigated a switched internal model approach to manage sinusoidal disturbances in nonlinear switched systems, focusing on improving adaptability and maintaining robust performance.

One of the applications that experiences multiple harmonic sinusoidal disturbances is the parkinsonian hand tremor. In Zhou et al. (2016), the characteristics of finger and wrist tremors were described. They identified that the frequencies of the first, second, and third harmonics of resting tremors across all joints were found to be between 3.5 Hz to 5.8 Hz, 6.9 Hz to 11.5 Hz, and 10.4 Hz to 17.3 Hz, respectively. The postural tremor's first to third harmonics fall between 3.9 Hz to 7.7 Hz, 7.7 Hz to 11.2 Hz, and 11.5 Hz to 16.8 Hz, respectively. In the tremor suppression device, our attention is solely directed towards suppressing involuntary motion, with no need to address voluntary motion. In Zhou et al. (2018), a method to suppress tremor signals was introduced, building upon the data provided in Zhou et al. (2016a). Their system comprises of sensors, actuation components, and a control system. IMU sensors are utilized to measure tremors at the wrist and joints of the fingers (specifically the thumb and index finger). The actuation system incorporates three brushless DC (BLDC) motors, each controlled by a commercial motor controller. Extracting the voluntary signal from the measured signal is essential for controlling the motion of patients' fingers and wrists. The effectiveness of the control system heavily relies on the accuracy of the tremor estimator, thus emphasizing the need for precise tremor estimation. In their study, they employed the Weighted-frequency Fourier Linear Combiner (WFLC) to estimate the tremor signal from the measurement signal before it is sent to the BLDC motor. The WFLC methodology was introduced by Riviere et al. (1998) and Veluvolu et al. (2007).

In Zhou et al. (2016b), the authors demonstrated the design and validation of a High-Order Weighted-Frequency Fourier Linear Combiner-based Kalman Filter for estimating parkinsonian tremors. They utilized the frequency tracking capability of two WFLCs, complemented by a Kalman Filter for better amplitude estimation. The results showed that the proposed algorithm had better tremor estimation performance than the WFLC. Additionally, the results highlighted the significant impact of the order of the Parkinsonian tremor model used in the Kalman Filter on estimation performance. However, This method was complicated for estimating the tremor signal from voluntary motion.

This motivates us to improve the control system to cancel specific frequencies within the bandwidth. Why is this study necessary? Based on previous research in tremor signal suppression, the goal is to suppress the tremor signal, defined as a sinusoidal signal, without affecting voluntary motion, which is defined as a non-sinusoidal signal. In this paper, we will test the Internal Model Principle (IMP) for rejecting periodic signals within a specific bandwidth. The algorithm relies on Field-Oriented Control (FOC) to generate torque signals (disturbances) on the shaft of a BLDC motor, which is then connected to another motor controlled by IMP and a common controller such as a PID controller or a lead-lag compensator.

This paper is organized as follows: the first section was an introduction that prefaced the topic of sinusoidal disturbances and their cancellation. The second section provides a brief literature review on BLDC motors. The third section details the setup of the experiment to control the torque on BLDC Motor 1 using FOC. The fourth section presents the design of the controller based on the experimental results using IMP to cancel disturbances in a specific bandwidth. In the fifth section the designed controller will be utilized to control Motor 2 to freeze Motor 1 or eliminate the fundamental frequency when we add the first harmonic to the disturbance signal. The sixth section presents the results and discussion. Finally, the seventh section concludes the paper and future works.

Literature Study of BLDC Motor

BLDC motors have evolved over the past 25 years through the integration of a compact motor, such as a permanent magnet stepper motor, with a rotor position sensor and an electronic switching circuit. Referred to as BLDC motors, they operate on DC power without the need for commutators and brushes. The fundamental elements of a BLDC motor consist of a permanent magnet rotor, a stator with windings comprising three, four, or more phases, a rotor position sensor, and an electronic control circuit to control the phases of the rotor winding.

BLDC motors have many advantages like being efficient, reliable, low-maintenance, quieter than brushed DC motors, and capable of high-speed operation. However, they can be pricier than regular DC motors because they use permanent magnets and need more complex controls (Edition & Chapman 2012).

In this study, we aim to control the torque of a BLDC motor to stop or reduce the rotation of the motor's shaft without causing any damage. Relying solely on voltage control may not provide the precise control required and could potentially damage the motor when attempting to stop it abruptly. We utilized FOC to control the torque of the BLDC motor. FOC involves adjusting the direct axis current (i_d) and the quadrature axis current (i_q) to achieve the desired torque (r_d). Further details about FOC can be found in Kronberg (2012), Sharma and Sindekar (2016), and Fadli et al. (2019). Figure 1 shows the FOC algorithm.

Figure 1. *Block Diagram of FOC*

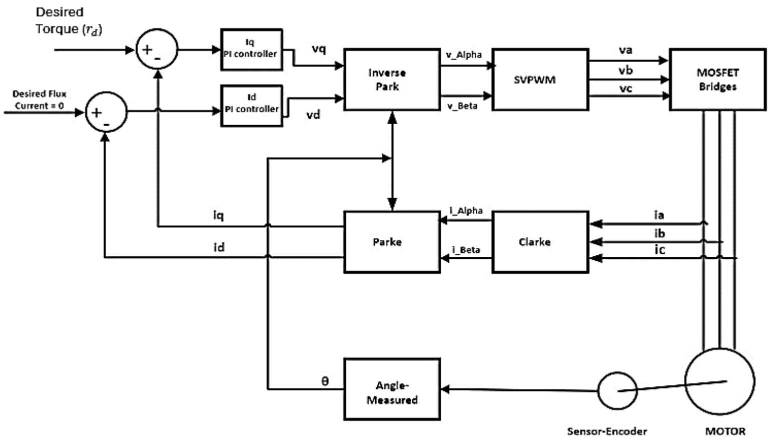

Experimental Setup For Torque Control

In this section, we present the required equipment needed to control the torque of BLDC Motor 1 based on the FOC algorithm. Figure 2 illustrates the setup of the system in the lab. The necessary equipment includes:

1) Microcontroller: The microcontroller used in this experiment is the STM32F446RE, shown in Figure 2. Developed by STMicroelectronics and based on the ARM Cortex-M4 core, it operates at a clock frequency of up to 180 MHz, providing high processing power. Additionally, the resolution of its analog-to-digital converters and digital-to-analog converters is 12 bits.
2) Motor Driver: In this experiment, we utilized the DRV8302 motor driver, developed by Texas Instruments, as shown in Figure 2. This driver requires a power supply of 24 V and a maximum current of 2 A. Additionally, the motor driver offers essential functions for motor control, including high and low side gate drivers, current sensing, and protection features.
3) BLDC Motor: The motor was used to control its torque or generate torque signals on its shaft. It has the following specifications: a rated voltage of 24 V, input power of 15 Watts, maximum speed of 480 RPM, and maximum torque of 2 Kg·cm. Additionally, this motor is equipped with two sensors: an encoder with a resolution of 4096 pulses per revolution and a Hall effect sensor.
4) AC/DC Adapter: The adapter was used to supply power to the motor driver. It has a maximum voltage and current of 24 V and 2 A respectively.

Figure 2. *Experimental Configuration for Torque Control: (A) STM32F446RE, (B) Motor Driver DRV8302, (C) BLDC Motor*

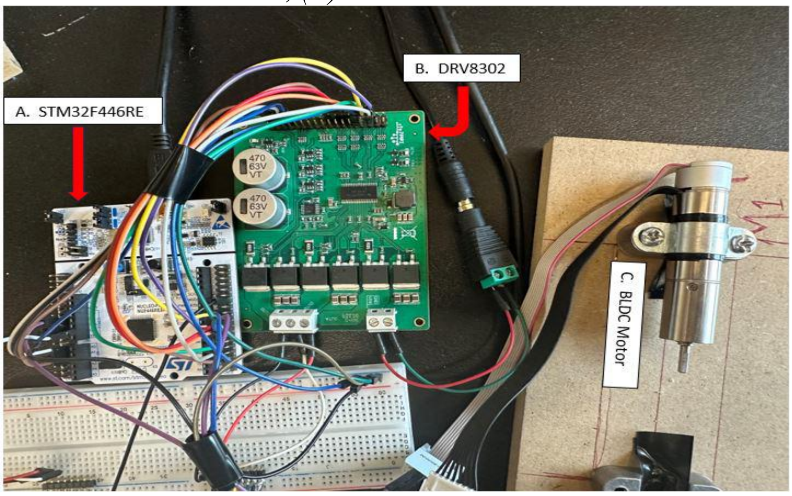

Deriving PI Control Parameters

The setup used to control the torque on the BLDC motor's shaft was connected as displayed in Figure 2. To achieve a desired torque (r_d) close to the actual torque (i_q), it is important to determine the PI controller parameters for the quadrature current (i_q) and direct current (i_d) accurately.

The Ziegler-Nichols method was employed for this purpose. This method aims to find the parameters of the PID controller through trial and error. The procedure involves initially setting the I and D gains to zero. Then, the P gain is gradually increased until it reaches a critical value, known as K_{cr}, at which the loop output begins to oscillate. The values of K_{cr} and the oscillation period, P_{cr}, are then used to adjust the gains accordingly (Erol et al. 2017).

$$K_p = 0.45K_{cr} \qquad T_i = \frac{P_{cr}}{1.2} \qquad (1)$$

Results from Torque Controller

From the Ziegler-Nichols technique, the parameters of the PI controller were determined as in Table I. In this experiment, we applied those parameters to control the torque circuit. The desired torque is set to increase from 0.05 A to 0.5 A and remain at 0.5 A for a period of time, then drop to 0.2 A and remain at that level for another period of time. No load was placed on the shaft.

Table 1. *PI Parameters*

Parameter	PI for $\boldsymbol{i_d}$	PI for $\boldsymbol{i_q}$
K_{cr}	22	44
P_{cr}	0.0629 s	0.06269 s
K_P	10	20
T_i	0.0522 s	0.0522 s

Figure 3 shows a comparison between the desired torque and the actual torque on the shaft. The black line represents the applied torque on the motor, while the red line shows the actual torque on the motor. It can be observed that the actual torque on the motor closely matched the applied torque. Additionally, the current on each phase (I_a, I_b, I_c) of the BLDC motor was measured, as shown in Figure 4. The maximum amplitude of each phase corresponded to the actual torque of the motor, and the angle between each phase was 120^o. This indicates that the torque applied to the motor was the desired torque.

Figure 3. *Controlling Torque in BLDC Motor Using FOC Algorithm*

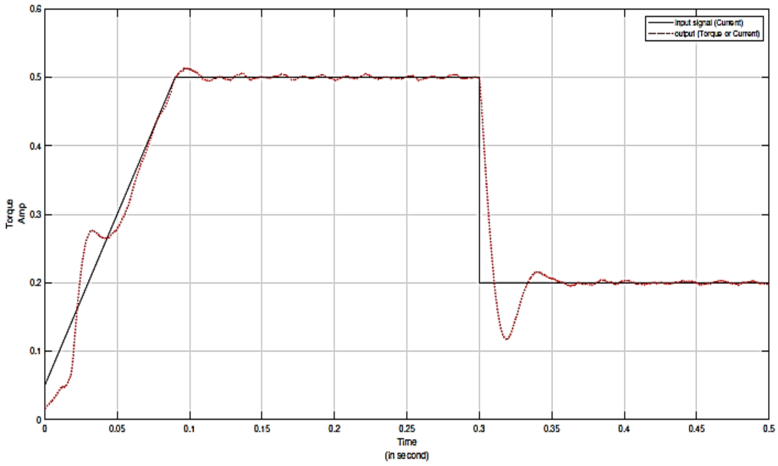

Figure 4. *Three-Phase Currents and Actual Torque of the BLDC Motor*

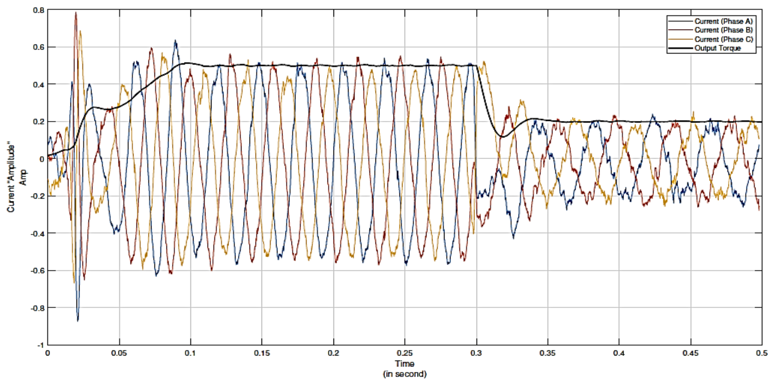

Determine the Transfer Function between the desired and the Actual Torque

We need to find the transfer function that describes how the desired torque relates to the actual torque. This will help us design the controller for controlling BLDC Motor 2 in the next step. In control engineering, the system identification technique is commonly used to establish the transfer function of a model. This method deals with black-box models of dynamical systems, where inputs and outputs can be measured (Ljung 2001). Based on this study, we can determine the transfer function since we have both input and output data. Upon observing Figure 3, we notice that the transfer function will be of second degree due to the presence of one overshoot. The second-degree transfer function is represented as follows:

$$H(s) = \frac{K_{DC} * \omega_n}{s^2 + 2\zeta\omega_n s + {\omega_n}^2} \tag{2}$$

$$K_{DC} = \frac{y(\infty)}{r(\infty)} \tag{3}$$

$$M_P = \frac{y(t_P) - y(\infty)}{y(\infty)} \tag{4}$$

$$\zeta = \sqrt{\frac{ln^2(M_P)}{ln^2(M_P) - \pi^2}} \tag{5}$$

$$\omega_n = \frac{\pi}{t_P\sqrt{1-\zeta^2}} \tag{6}$$

In the equations, K_{DC} represents the steady-state gain, denoted as the DC gain. Here, $y(\infty)$ and $r(\infty)$ represent the DC values of the output and input, respectively. Additionally, M_P denotes the overshoot, t_P stands for the peak time, while ω_n represents the natural radian frequency, and ζ signifies the damping ratio.

When utilizing the system identification method to determine the parameters of the transfer function, the values of K_{DC}, ζ and ω_n are found to be 1, 0.37 and 192.11 rad/sec, respectively. The transfer function between desired torque and actual torque is:

$$\frac{i_q}{r_d} = \frac{3.691X10^4}{s^2 + 142.6s + 3.691X10^4} \tag{7}$$

We validated the accuracy of the transfer function using Matlab by applying the same input signal as shown in Figure 3. Figure 5 represents a comparison between the motor's response and the output of the transfer function. Both outputs demonstrate an identical response, confirming the validity of the transfer function.

Figure 5. *Comparison of Desired Torque and Actual Torque from Motor with Transfer Function*

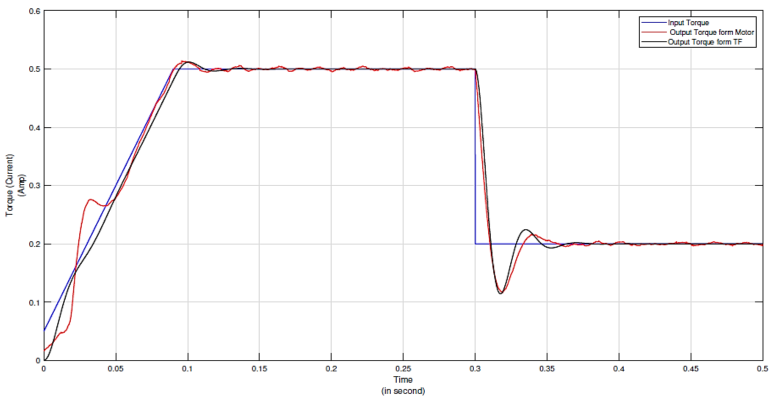

The Proposed Technique Based on IMP

The IMP, developed by Francis and Wonham in 1976, is a well-known approach for reducing periodic disturbances in control systems. In a feedback system, the IMP aims to introduce closed-loop transmission zeros that counterbalance the critically stable poles linked to disturbance and/or reference signals (Francis & Wonham 1976). In Mohsen, Brown and Chen (2017), the authors introduce a new tuning approach for an adaptive IMP based signal identification algorithm. The algorithm was designed with a bandpass filter with notches at specific frequencies within the bandwidth of the filter. Based on this study, we aim to cancel the disturbance signal within a narrow bandwidth without an effect on others. Figure 6 shows the block diagram of the controller utilized for canceling specific frequencies of the disturbance signal.

Figure 6. *Control System Architecture*

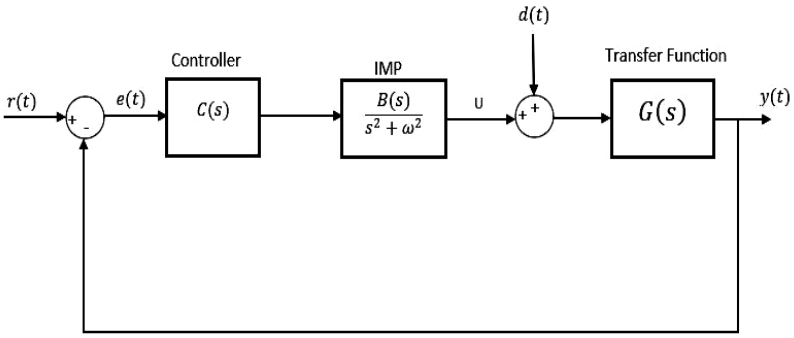

From the third section, we determined the transfer function representing the relationship between input torque and actual torque. Therefore, G(s) corresponds to the transfer function as defined in Equation 7. In the IMP, the numerator B(s) takes the form $s + \omega$, where ω denotes the frequency targeted for cancellation. Meanwhile, C(s) denotes a generic controller, such as a P Controller, PI Controller, PID Controller, or lead lag compensator. In this study, C(s) is configured as the P controller with P = 5.

The closed-loop transfer function from d(t) to y(t) in Figure 6 will be represented by the following equation:

$$\frac{Y(S)}{D(s)} = \frac{G(s)}{1 + C(s)G(s)IMP(S)} \tag{8}$$

We assume there is a sinusoidal disturbance signal given by $d(t) = 0.7\sin(2\pi x1t)$. Since we do not need to track any signal, the reference signal r(t) is set to zero. We choose ω in the IMP to match the disturbance frequency, and we plot the Bode diagram of the closed-loop transfer function for Equation 8. Figure 7 shows the Bode plot.

Figure 7. *Bode Plot of the Transfer Function* $\frac{Y(S)}{D(s)}$

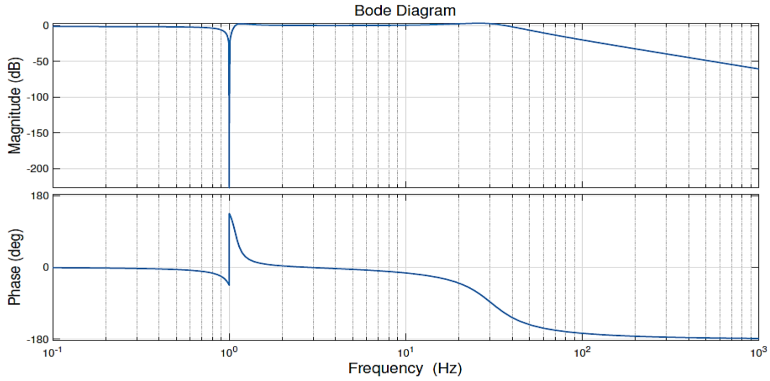

Based on the frequency response analysis, the system behaves as a low-pass filter with a cutoff frequency of approximately 40 Hz, where the magnitude plot decreases by -3 dB from its peak value. Within this specific bandwidth, the algorithm should cancel the disturbance at the frequency ω specified by the IMP and disregard other frequencies.

Simulation Result and Discussion

If the disturbance comprises a single frequency, the algorithm will effectively suppress it. The algorithm's response to this disturbance is illustrated in Figure 8. However, if an additional harmonic is added, it falls within the bandwidth shown in Figure 7. Consequently, the disturbance transforms into $d(t) = 0.7\sin(2\pi x1t) + 0.3\sin(2\pi x2t)$.

Figure 8. *Algorithm Response at Single Frequency*

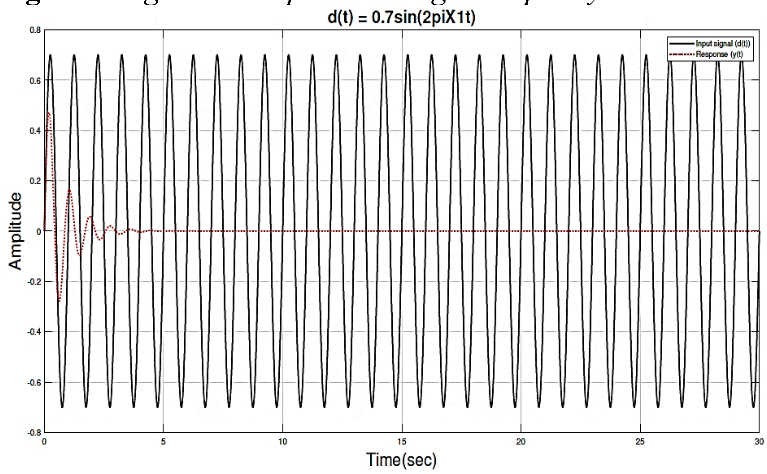

Figure 9 illustrates the response to a disturbance signal containing a harmonic. The black wave represents the disturbance signal with a fundamental frequency of one Hz and a harmonic at two Hz. The red wave shows the actual response. The outcome demonstrates cancellation of the fundamental frequency, while the first harmonic appears in the response with the same frequency and amplitude. This simulation showcases the ability to cancel specific frequencies while ignoring others, as long as they fall within a specified bandwidth. In the next section, we will validate these findings experimentally.

Figure 9. *Algorithm Response at Fundamental Frequency and its First Harmonic*

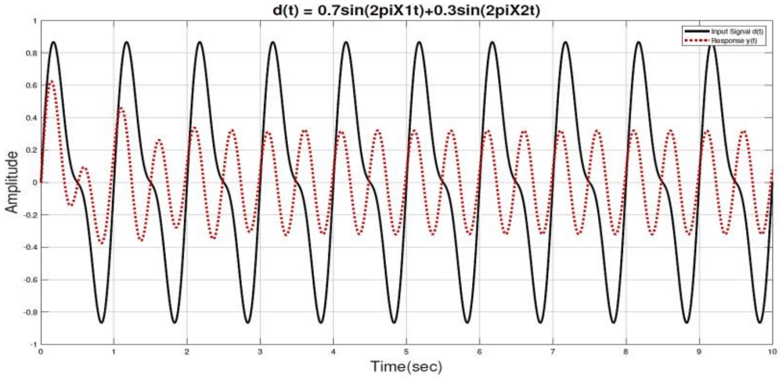

Experimental Validation: A Practical Study

In this section, we introduce the experimental configuration comprising an extra motor (Motor 2), a motor driver, and a microcontroller. These elements have similar the specifications to those used in the torque control experiment discussed in the third section. Figure 10 illustrates the experimental setup on the bench-top. In this experiment, we have two circuits: the torque control circuit, which produces disturbances on the shaft of Motor 1, and the control circuit for disturbance cancellation. We applied the algorithm explained in the fourth section to regulate the speed of Motor 2. Two motors are connected by a coupler. The torque circuit represents as an open loop control system relative to the disturbance cancellation circuit.

Figure 10. *Visualization of the Experimental Setup – Showing Two Circuits (A. Control Torque Circuit) and (B. Control Circuit for Disturbance Cancellation*

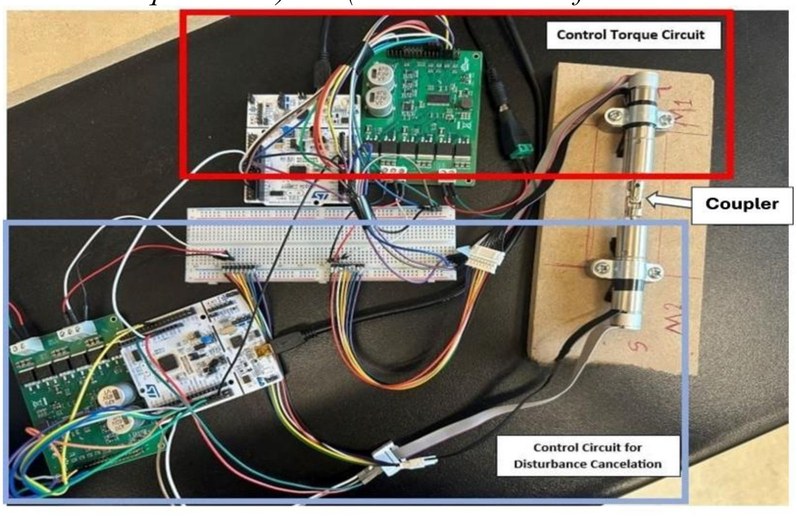

The aim of this experiment is to assess whether the angular velocity of Motor 2 synchronizes with that of Motor 1 when a sinusoidal torque is applied to Motor 1, with the disturbance cancellation circuit deactivated. Additionally, we investigate whether activating the disturbance cancellation circuit allows Motor 2 to freeze Motor 1 in the presence of a fundamental frequency disturbance or to eliminate the harmonic frequency when the disturbance includes both the fundamental and first harmonic.

Results and Discussion

For further clarification, the results of the experiment are divided into two sections: Section A examines the scenario where only a sinusoidal torque signal with the fundamental frequency is applied to Motor 1, representing a disturbance signal on Motor 2. In Section B, a first harmonic is added to the sinusoidal torque signal applied to Motor 1, also acting as a disturbance signal on Motor 2.

A. Results for Fundamental Frequency Disturbance

We applied a sinusoidal torque signal to Motor 1, containing only the fundamental $r_d(t) = 0.7\sin(2\pi x 1t)$. Then, we measured the angular velocities of both Motor 1 and Motor 2 with the controller algorithm for Motor 2 turned off. The results indicate that when Motor 1 initiates rotation due to torque applied at one Hz, the shaft of Motor 2 also begins to rotate, matching the angular velocity of Motor 1. Upon measuring the angular velocity of both motors, it was observed that the frequency was nearly one Hz. Figure 11 illustrates the comparison of angular velocities between the two motors. The black waveform represents the measured angular velocity from Motor 1, while the red waveform represents that from Motor 2.

Figure 11. *Comparison of Angular Velocities between Motor 1 and Motor 2 without the Cancellation Algorithm*

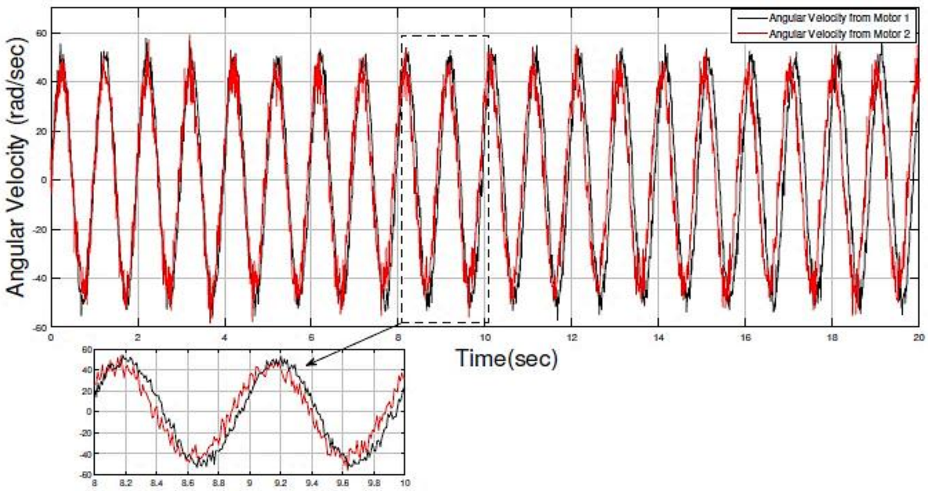

After investigation, it was determined that Motor 2 can replicate the angular velocity of Motor 1. Upon activating the cancellation circuit's algorithm, Motor 2 can freeze Motor 1. The results illustrated in Figure 12 show that the angular velocity of Motor 1, represented by the red waveform, decreases to zero. This indicates that the cancellation algorithm effectively freezes Motor 1.

Figure 12. *Measurement of Angular Velocity from Motor 1 before (Black Waveform) and after (Red Waveform) Cancellation*

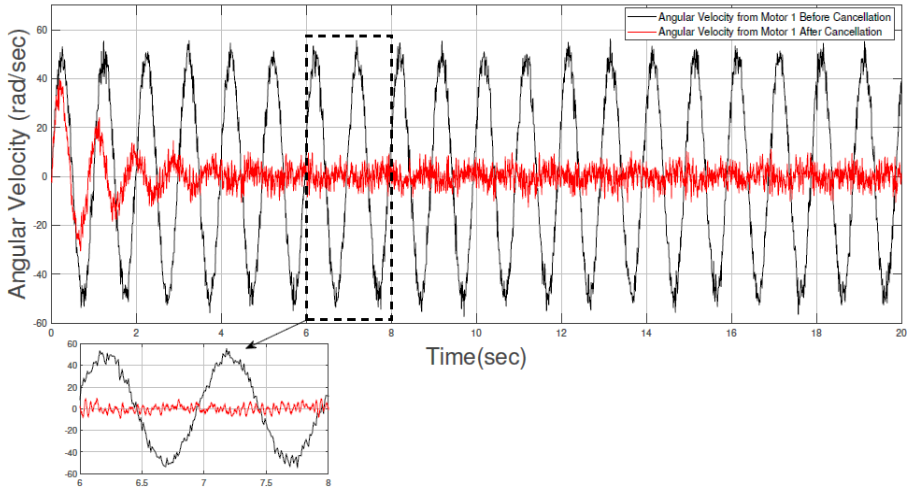

B. Results for the Disturbance with a Fundamental Frequency and First Harmonic

We added a first harmonic to the torque signal applied to Motor 1 $r_d(t) = 0.7\sin(2\pi x1t) + 0.3\sin(2\pi x2t)$. Figure 13 displays the angular velocities measured by the encoders of Motor 1 (illustrated in black waveform) and Motor 2 (illustrated in red waveform) when the disturbance cancellation circuit was inactive. Analyzing the measurement signal using FFT, as shown in Figure 14, identified two frequency components: a fundamental frequency and its first harmonic, that corresponds to the applied torque frequency signal.

Figure 13. *Comparison of Angular Velocities between Motor 1 and Motor 2 without the Cancellation Algorithm when First Harmonic is Added*

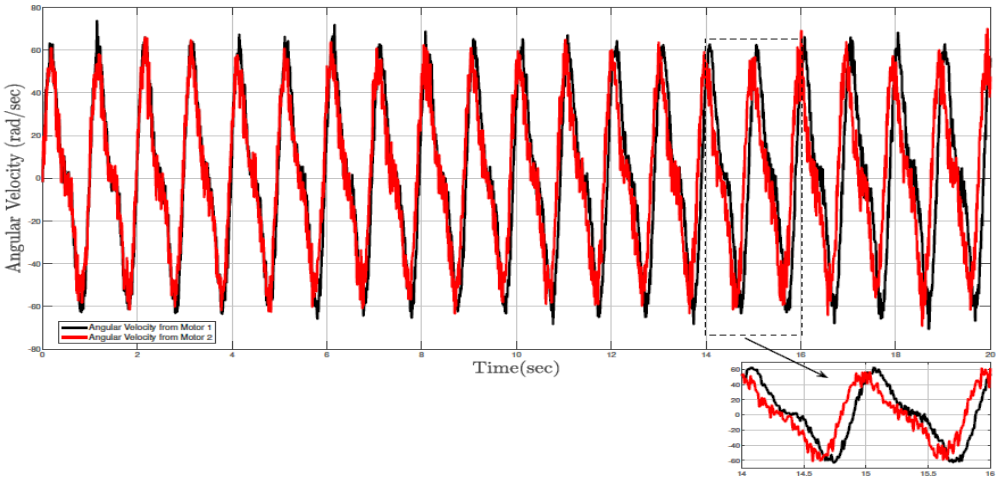

Figure 14. *Visualization of the FFT of Angular Velocity Data Obtained from Motor 1 and Motor 2 before Cancellation*

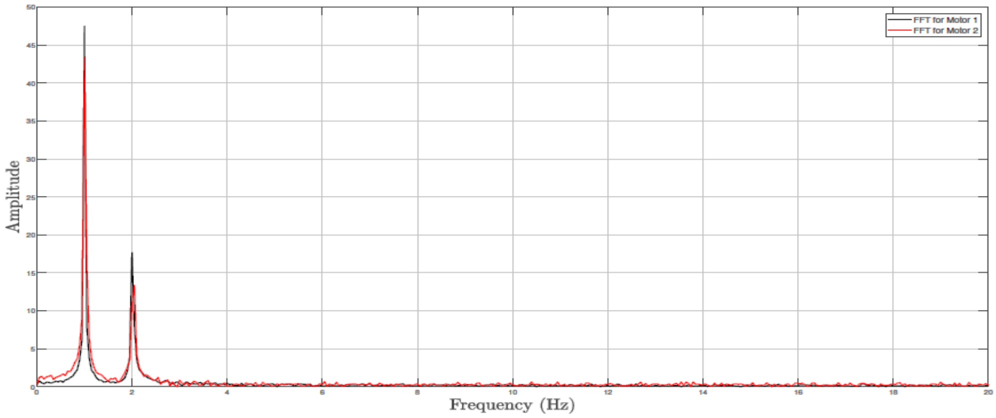

When the cancellation circuit's algorithm was activated, Motor 2 began to suppress the fundamental frequency, as shown in Figure 15. However, Motor 1 did not stop completely; it continued to rotate at the frequency of the first harmonic of the applied torque signal. Additionally, analyzing the FFT of the output signal from Motor 1 after the cancellation circuit was activated showed that the remaining frequency was two Hz. This equals the first harmonic of the applied torque shown in Figure 16.

Figure 15. *Angular Velocity Measurements from Motor 1 before (Black Waveform) and after (Red Waveform) Activation of Cancellation when First Harmonic is Added*

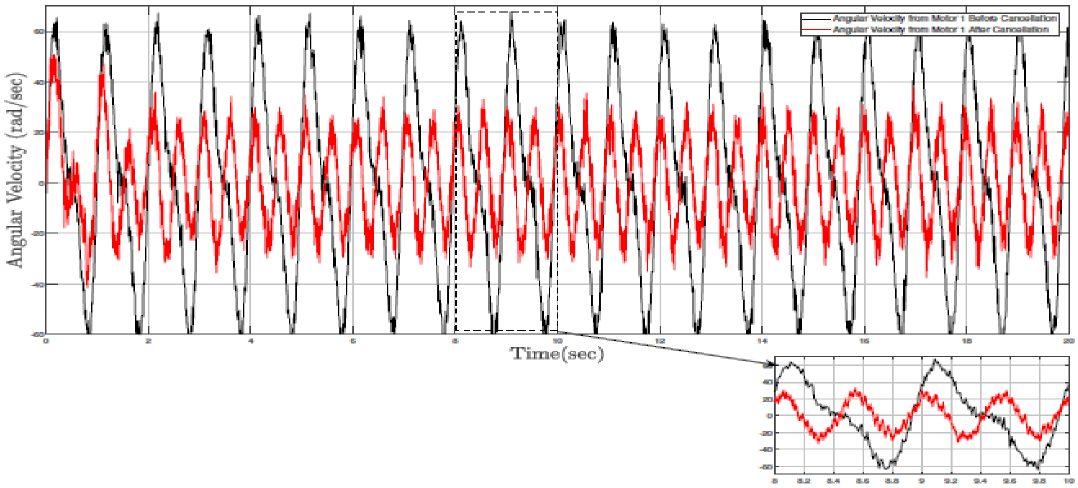

Figure 16. *Visualization of FFT of Angular Velocity Data Obtained from Motor 1 after Cancellation*

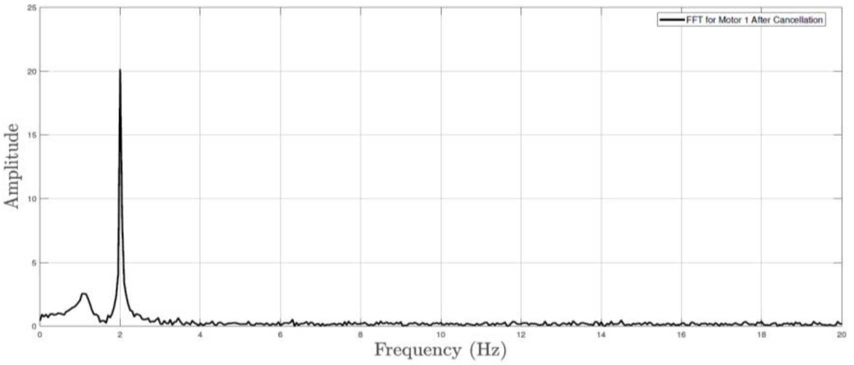

Conclusion and Future Work

This work proposes the implementation of a system to cancel sinusoidal disturbance signals within a narrow bandwidth. The objective of this research was to eliminate a specific frequency without affecting other frequencies within the same bandwidth. The study combines FOC of motors with the IMP. The simulation results demonstrated the ability to cancel a specific frequency within a given bandwidth without impacting other frequencies.

In the experimental setup, two motors were used to implement the proposed algorithm. Motor 1 was controlled by FOC to control torque on its shaft, simulating the introduction of a disturbance. Motor 2, controlled by the proposed IMP-based algorithm, aimed to cancel the unwanted frequencies generated by Motor 1. The experimental results illustrated that Motor 2 could successfully cancel the targeted frequency while leaving other frequencies unaffected, validating the effectiveness of the proposed approach in practical applications.

Future work will concentrate on the development of advanced algorithms for the cancellation of sinusoidal disturbance signals through the on-line tuning of the parameters of the controller in real time. This will involve defining the narrow bandwidth to effectively eliminate the targeted frequencies within that range. The aim is to enhance the precision and robustness of frequency cancellation while maintaining the integrity of non-targeted frequencies within the specified bandwidth.

References

Bodson M, Douglas SC (1997) Adaptive algorithms for the rejection of sinusoidal disturbances with unknown frequency. *Automatica* 33(12): 2213–2221.

Brown LJ, Zhang Q (2004) Periodic disturbance cancellation with uncertain frequency. *Automatica*, 40(4): 631–637.

Edition F, Chapman SJ (2012) Electric machinery fundamentals.

Erol O, Aktaş M, Altun Y (2017) Obtaining of PI control parameters for vector controlled PMSM. In *Proc. Int. Conf. Hydraul. Pneum. Tools, Seal. Elem. Fine Mech. Specif. Electron. Equip. Mechatronics*.

Fadli MR, Musyasy MM, Furqani J, Purwadi A (2019, November) Modelling of field orientation control (FOC) method in 120 kW brushless DC motor (BLDC). In *2019 6th International Conference on Electric Vehicular Technology (icevt)*, 383–389. IEEE.

Francis BA, Wonham WM (1976) The internal model principle of control theory. *Automatica* 12(5): 457–465.

Kamaldar M, Hoagg JB (2021) Centralized and decentralized adaptive harmonic control for sinusoidal disturbance rejection. *Control Engineering Practice* 112: 104814.

Kronberg A (2012) Design and simulation of field oriented control and direct torque control for a permanent magnet synchronous motor with positive saliency. Available at: https://www.semanticscholar.org/paper/Design-and-Simulation-of-Field-Oriented-Control-and-Kronberg/35d4381596d336c6802148cdd7674551fe7f1d32.

Ljung L (2001, May) Black-box models from input-output measurements. In *IMTC 2001. Proceedings of the 18th IEEE instrumentation and measurement technology conference. Rediscovering measurement in the age of informatics (Cat. No. 01CH 37188)*. Vol. 1, 138–146). IEEE.

Long L (2021) Global disturbance rejection of switched nonlinear systems with switched internal model. *Journal of Systems Science and Complexity* 31(1): 161–172.

Madonski R, Stanković M, Shao S, Gao Z, Yang J, Li S (2020) Active disturbance rejection control of torsional plant with unknown frequency harmonic disturbance. *Control Engineering Practice* 100: 104413.

Mohsen E, Brown LJ, Chen J (2017) A Real time Alternative to the Hilbert Huang Transform Based on Internal Model Principle. *J Electr Electron Syst* 6(233): 2332–0796.

Pigg S, Bodson M (2009) Adaptive algorithms for the rejection of sinusoidal disturbances acting on unknown plants. *IEEE Transactions on Control Systems Technology* 18(4): 822–836.

Pigg S, Bodson M (2011, June) A new algorithm for frequency estimation and disturbance cancellation inspired from induction machine theory. In *Proceedings of the 2011 American Control Conference*, 3018–3023. IEEE.

Pigg S, Bodson M (2013) Adaptive harmonic steady-state disturbance rejection with frequency tracking. *Asian Journal of Control* 15(1): 1–10.

Riviere CN, Rader RS, Thakor NV (1998) Adaptive cancelling of physiological tremor for improved precision in microsurgery. *IEEE Transactions on Biomedical Engineering* 45(7): 839–846.

Sharma PK, Sindekar AS (2016, December) Performance analysis and comparison of BLDC motor drive using PI and FOC. In *2016 International Conference on Global Trends in Signal Processing, Information Computing and Communication (ICGTSPICC)*, 485–492. IEEE.

Veluvolu KC, Tan UX, Latt WT, Shee CY, Ang WT (2007, August) Bandlimited multiple fourier linear combiner for real-time tremor compensation. In *2007 29th Annual International Conference of the IEEE Engineering in Medicine and Biology Society*, 2847–2850. IEEE.

Wen X, Yan P (2020) Disturbance-prediction–based control of input time delay systems for rejection of unknown frequency disturbances. *International Journal of Robust and Nonlinear Control* 30(1): 338–350.

Zhou Y, Jenkins ME, Naish MD, Trejos AL (2016, August) Design and validation of a high-order weighted-frequency fourier linear combiner-based Kalman filter for parkinsonian tremor estimation. In *2016 38th Annual International Conference of the IEEE Engineering in Medicine and Biology Society (EMBC)*, 5893–5896. IEEE.

Zhou Y, Jenkins ME, Naish MD, Trejos AL (2016, February) The measurement and analysis of Parkinsonian hand tremor. In *2016 IEEE-EMBS International Conference on Biomedical and Health Informatics (BHI)*, 414–417. IEEE.

Zhou Y, Jenkins ME, Naish MD, Trejos AL (2018, August) Development of a wearable tremor suppression glove. In *2018 7th IEEE International Conference on Biomedical Robotics and Biomechatronics (Biorob)*, 640–645. IEEE.